Radiative heat transfer in free-standing silicon nitride membranes in the application of thermal radiation sensing

Chang Zhang

Thesis submitted to the University of Ottawa
in partial fulfillment of the requirements for the degree of

MASTER OF APPLIED SCIENCE

Department of Mechanical Engineering
Faculty of Engineering
University of Ottawa

Abstract

Thin-film silicon nitride (SiN) membranes mechanical resonators have been widely used for many fundamental opto-mechanical studies and sensing technologies due to their extremely low mechanical dissipation (high mechanical Q-factor). In this work, we experimentally demonstrate an opto-mechanical approach to perform thermal radiation sensing, using a SiN membrane resonator. An important aspect of this work is to develop a closed-form analytical heat transfer model for assessing the thermal coupling condition between free-standing membranes and their environment. We also derive analytical expressions for other important intrinsic thermal quantities of the membrane, such as the thermal conductance, the heat capacity and the thermal time constant. Experimental results show good agreement with our theoretical prediction. Of central importance, we show that membranes of realistic dimensions can be coupled to their environment more strongly via radiation than by solid-state conduction. For example, membranes with 100 nm thickness (frequently encountered size) are predicted to be radiation dominated when their side length exceeds 6 mm. Having radiation dominated thermal coupling is a key ingredient for reaching the fundamental detectivity limit of thermal detectors. Hence, our work proves that SiN membranes are attractive candidates for reaching the fundamental limit. We also experimentally exhibit the high temperature responsivity of the SiN membranes resonance, in which we shift a 88.7 KHz resonance by over 1 KHz when temperature increment on the membrane is approximately 2 K.

Acknowledgments

I would like to express my sincere gratitude to the ones who helped to make this work possible. First, I would like to thank my supervisor Prof. St-Gelais who spent great amount of time and effort to guide me in the course of this project. In addition, I would like to thank all of my current and former colleagues who helped me in the experimental perspective of things. Thea Abdul Nour setup the vacuum environment, Mathieu Giroux characterized the ceramic heater in the experiment and Dr. Huan Huang provided constructive suggestions for the experimental design. Without these individuals, this work would not have been possible.

Contents

List of Figures

1. Introduction

1.1 Working principle & limitation of the traditional bolometer

Bolometers are the popular choice for measuring light and infrared radiation. Traditional bolometers [see Fig. (1.1)] rely on electrical sensing mechanism. As the sensor absorbs thermal radiation, its temperature rises. Meanwhile, it generates a voltage difference due to the change of resistance. The absorber on a traditional bolometer serves both as a radiation absorber and as an electrical component of the readout circuit. From a thermal perspective, the absorber must be as isolated as possible from its supporting substrate (i.e., large thermal resistance) such that the temperature fluctuation noise [1] is minimized and the thermal effect of radiation is as strong as possible. From an electrical perspective, the absorber must be as electrically conductive as possible (i.e., small electrical resistance), which helps to minimize electrical Johnson noise. Nevertheless, it is impossible to find a material that can achieve both large thermal resistance and small electrical resistance at the same time due to the fact that these two resistances are always proportional to each other in virtually any material [2]. Thus, electrical sensing scheme introduces a performance trade-off (between low electrical resistance and high thermal resistance) in traditional bolometers. This trade-off prevents bolometers from reaching the fundamental performance limit of thermal radiation sensors, known as the fundamental detectivity limit, which is two orders of magnitude higher than the current sensors [3]. Here, the fundamental limit means when the device is solely affected by temperature fluctuation generated by thermal radiation.

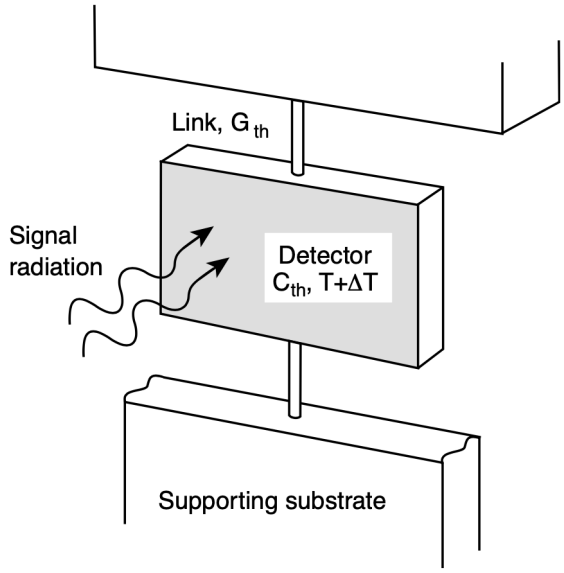

Figure 1.1: *Schematic of traditional bolometer [3].*

1.2 Objective & scope of this work

To break this trade-off (i.e., eliminating Johnson noise), previous works used mechanical [4, 5, 6] and optical [7] microresonators for performing thermal radiation sensing. By relying on optical or mechanical resonances to measure temperature, electrical Johnson noise is eliminated and the performances can be optimized by minimizing thermal conductance. However, there is still no evidence of radiation sensors operating at the fundamental detectivity limit. This is largely due to the fact that the thermal coupling of the absorbers is not dominated by thermal radiation in previous works [4, 5, 6]. Specifically, to reach the fundamental limit of a physical bolometer, the absorber must be thermally coupled with the environment more strongly via radiation (i.e., radiation-dominated thermal coupling) than other types of heat transfer (e.g., solid-state conduction and convection) such that the thermal noise of bolometer is mainly contributed by background thermal radiation exchange.

The long-term goal of this project is to demonstrate thermal radiation sensing at the fundamental detectivity limit using mechanical resonators consisting of thin-film SiN

[8, 9, 10]. These resonators are widely known for their ultra-high mechanical Q-factor and can easily be fabricated with a variety of dimensions.

However, this is still no analytical heat transfer model for evaluating the thermal coupling condition of a thin-film absorber. Thus, the specific objective and the main contribution of this work is to provide an analytical solution for assessing whether thermal coupling of a regular shaped (e.g., circular and square) thin-film SiN membrane can be radiation dominated as a function of its dimensions (e.g., side length, radius, and thickness). This analytical approach also helps to find the mathematical expressions of important parameters in a thermal system such as the overall conductance G (W/K) and the thermal time constant τ of a SiN membrane. To provide experimental validation for the heat transfer model, we establish an experiment to perform thermal radiation sensing using a thin-film SiN membrane in a high-vacuum chamber. It should be noted that while this experimental confirms the validity of our heat transfer model, it does not yet allow the demonstration of radiation sensing at the fundamental detectivity limit. This long-term objective is still subject of effort by our group, using a different experimental approach. The heat transfer model and the experimental validation of this work are published as a research article in the Physical Review Applied journal [11].

1.3 Thermal radiation sensing using a thin-film SiN

Free-standing silicon nitride (SiN) thin-film membranes are the popular candidates for multiple applications due to their exceptional mechanical properties (i.e., extremely low dissipation, high mechanical Q-factor). They are widely used for studying coupling between optical and mechanical forces in fundamental opto-mechanical studies [8, 9, 10], and also other sensing applications, which include ultra-sensitive mass sensing [12], nanoparticulate matter detection [13], gas detection [14], and thermal radiation sensing [4, 15].

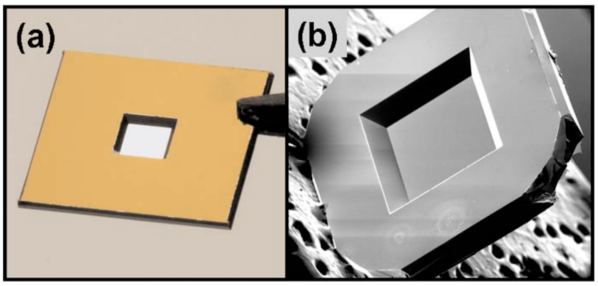

Figure 1.2: *Photograph of Norcada X-Ray membrane [16].*

In this work, we use a laser interferometer to detect the temperature-dependant mechanical resonance shift [17] of a thin-film SiN membrane. As the temperature of the SiN membrane changes, the internal stress changes simultaneously due to the thermal expansion effect. The variation in stress leads to resonance frequency shift of the membrane [see Fig. (1.3)]. We can relate the resonance shift to absorbed radiation intensity, and hence to perform thermal radiation sensing. Using this approach, the absorber (i.e., free-standing SiN membrane) does not serve as an electrical component in a read-out circuit and consequently breaks the performance trade-off exhibited by the traditional bolometers. Due to the opto-mechanical readout approach, we are now able to make the SiN membrane as thermally isolated from its substrate as possible via solid-state conduction (i.e., radiation-dominated thermal coupling), without adding electrical noise, as would happen in a conventional bolometer.

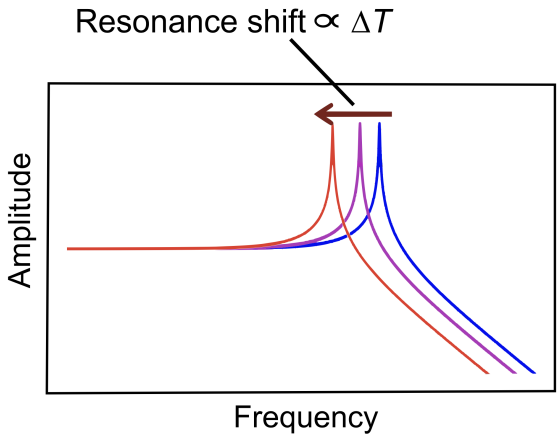

Figure 1.3: *Schematic of temperature-dependant resonance shift.*

2. Literature Review

Fig. (2.1) is a conventional performance benchmark of different types of radiation detectors, including photodetectors, bolometers and thermopiles. The Y-axis of Fig. (2.1) is the measure of specific detectivity D^* ($\mathrm{cmHz^{1/2}W^{-1}}$) which is the reciprocal of the noise equivalent power NEP ($\mathrm{W/Hz^{1/2}}$), normalized by the dimension ($\sqrt{\mathrm{Area}}$, in cm) of the absorber. In other words, a better detector exhibits a higher D^*.

Photodetectors and thermal detectors (e.g., thermopiles and bolometers) are the two main categories of radiation detectors. Photodetectors rely on either the photoconductive (i.e., impinging light creates free-charge carriers in semiconductor materials which translates into a change in resistivity) or photovoltaic effects (i.e., impinging light creates free-charge carriers in semiconductor materials, which translates into a change in electrical potential). The theoretical detectivity limits of photodetectors are generally higher than that of thermal detectors, but cryogenic cooling is necessary for most of the photodetectors to reach such high performance [see Fig. (2.1)], which increases the complexity.

In contrast, thermal detectors (i.e., focus of this work) measure temperature, based on the temperature-dependent properties of the sensing element when it absorbs thermal radiation. Note in Fig. (2.1) that D^* of the traditional thermistor bolometer (2×10^8 $\mathrm{cmHz^{1/2}W^{-1}}$) is in two orders of magnitude lower than the ideal thermal detector (2×10^{10} $\mathrm{cmHz^{1/2}W^{-1}}$) due to the performance trade-off discussed in the previous section.

In this literature review, we first review the characteristics of different types of classical thermal detectors (Section 2.1). We then investigate mechanical resonator-based thermal detectors (Section 2.2) in which are similar to our work, attempt to break the traditional performance trade-off using mechanical resonators instead of the classic electrical sensing schemes.

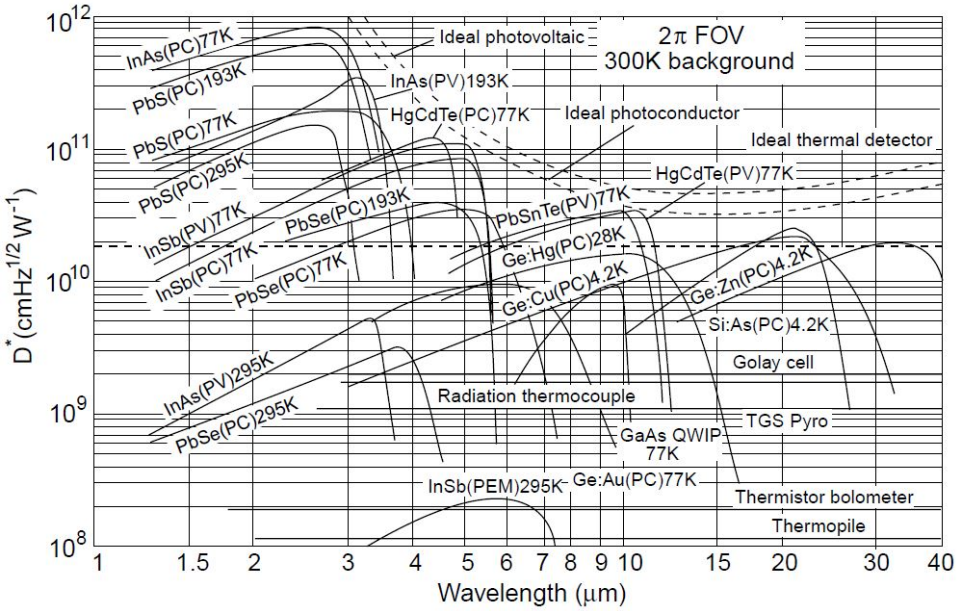

Figure 2.1: *Comparison of the specific detectivity for different types of detectors [3].*

2.1 Traditional thermal detector

2.1.1 Thermopile

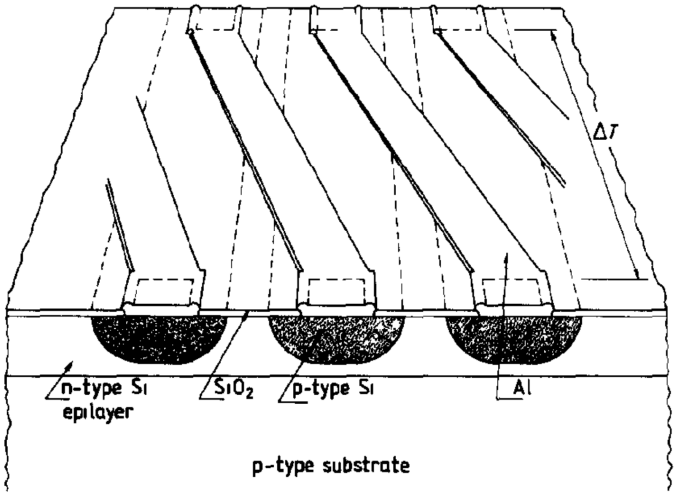

Figure 2.2: *Schematic of a silicon/aluminum thermopile [18].*

The thermopile can be regarded as the oldest type of thermal radiation detector which exhibits poorer detectivity and overall performance in comparison with the bolometer. However, it still has a firm position in nowadays thermal sensing market due to its low cost and great manufacturability, thanks to the rapid development of semiconductor and integrated circuit. The beginning of thermopile can be traced back to the discovery of the Seebeck effect – i.e., the proportionality relation between the voltage difference and the temperature difference at the junction of two distinct conductive materials. Using this effect, thermocouples are developed simply by connecting two different pieces of conductive materials in junction. However, the Seebeck coefficients are on the order of μV/K for virtually any conductive material. Thus, the voltage outputs are extremely small (e.g., on the order of some μV/K) when solely using a single unit of thermopile for thermal detection. To obtain a larger voltage readout when exposing to the change in temperature, thermopiles are created by connecting multiple thermocouples in series. In this case, thermopiles are designed to have far more temperature sensitivity than single thermocouple and can be used in infrared sensors due to a substantially larger readout value.

2.1.1.1 Thermoelectric properties of semiconductors

Modern thermopiles are usually made of semiconductor such as single-crystal silicon and poly-silicon due to their high Seebeck coefficients and can be conveniently fabricated by standard integrated circuit processes. In contrast, metals exhibit one or two magnitude lower Seebeck coefficients than semiconductors [19], which makes them the less favorable material for this particular application. In addition to the superior thermoelectric property, semiconductors Seebeck coefficients also exhibit less unwanted temperature dependency [19]. This means that semiconductor bolometers can be calibrated to operate linearly over a large temperature difference. Another major advantage of using semiconductor material for thermopile is that the Seebeck coefficient of a semiconductor can be engineered by altering its doping concentration level [see Fig. (2.3)] (e.g., a high doping

concentration level leads to a low electric resistivity and also a low Seebeck coefficient). Doping is a process of adding impurity to the silicon as it is being grown. The most common types of doped silicon are n-type (i.e., doped by either phosphorus or arsenic) and p-type (i.e., doped by either boron or gallium).

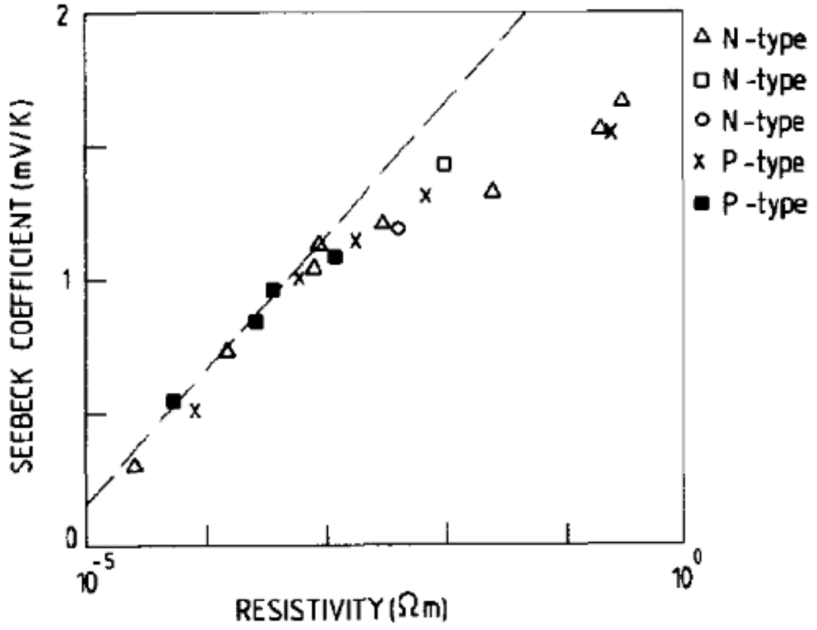

Figure 2.3: *Seebeck coefficients as a function of resistivity for multiple types of doped mono-crystalline silicon at 300 K. Different symbols for the same type of doped silicon (e.g., N-type or P-type) represent different types of dopants. The detailed information of the dopant material is not given in the paper [18].*

2.1.1.2 Design considerations

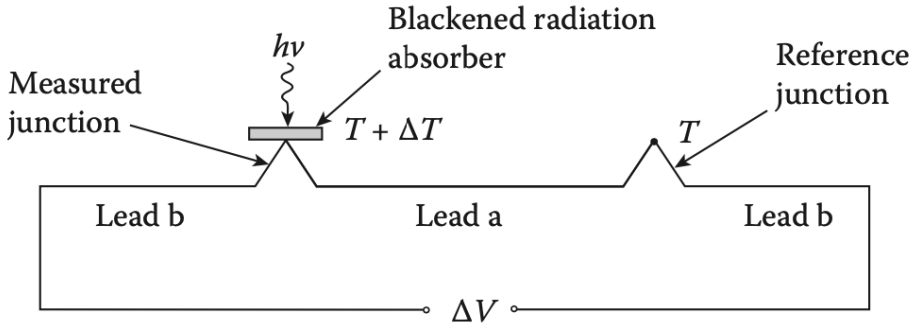

Figure 2.4: *Schematic of two dissimilar leads thermopile [3].*

One of the major requirements for a thermopile to operate at its desire state is to maintain a stable temperature difference ΔT between the measured junction (i.e., hot junction) and the reference junction (i.e., cold junction) such that the thermopile can produce a stable voltage readout. To achieve this, the reference junction must be highly insulated from its environment which ensures the reference junction temperature to remain unchanged during the measurement.

Note that as it is shown in Fig. (2.4), the conductor "Lead a" connects the measured junction and the reference junction together. Due to the solid-state conduction, heat flux can be transferred from the hot junction to the cold junction, which changes the temperature gradient slowly over time. This effect causes instability and inaccuracy for the measurement. However, nowadays thermopiles are usually made of poly-silicon that has low thermal conductivity, which minimizes the change in temperature gradient during the measurement. Moreover, the absorbing panel which connects with the measured junction must have high emissivity (e.g., usually blackened) and low heat capacity such that the measured junction can be thermally more connected to the sensing object via radiation and has a fast thermal response.

As a consequence of the thermoelectric sensing scheme, the materials of junctions are required to be highly electrically conductive in order to generate sufficient value in readout and minimize electric Johnson noise. However, a high electric conductivity leads to a low Seebeck coefficient [see Fig. (2.5)] (i.e., the Seebeck coefficient and the resistivity of a material are inversely proportional). This is the classic performance trade-off for any thermopile which relies on thermoelectric properties of the materials to generate readout. Hence, to mitigate this trade-off, the figure of merit for thermoelectric materials is defined as Eq. (2.1) [1]:

$$Z = \frac{(\alpha_a - \alpha_b)^2}{\sqrt{\rho_a G_a} + \sqrt{\rho_b G_b}}, \tag{2.1}$$

where α represents the Seebeck Coefficient (μV/K), ρ is the electric resistivity (Ω), and G (W/m $\cdot$ K) is the thermal conductance. It is shown in Fig. (2.5) that semiconductors

generally have the highest Z value, hence perform better in thermal radiation sensing than metals and other materials.

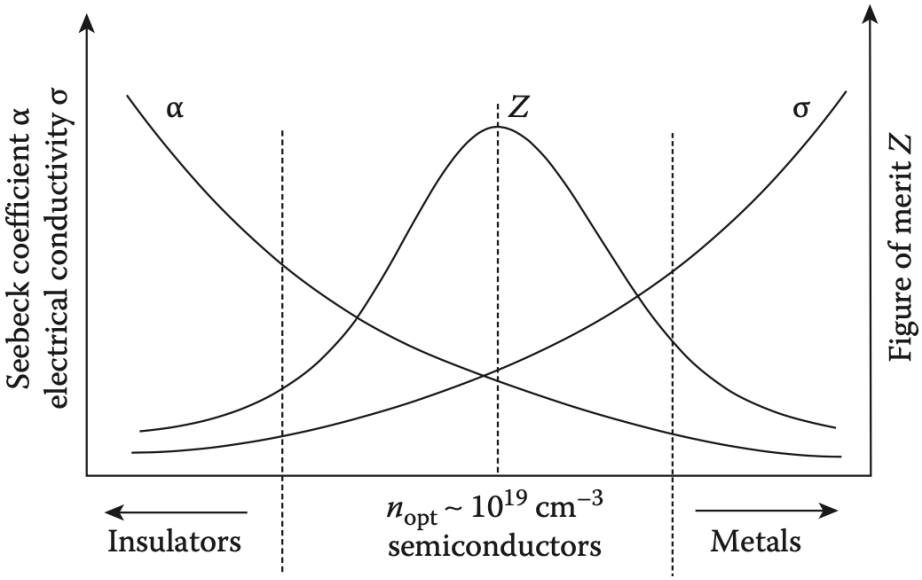

Figure 2.5: *Thermoelectric figure of merit for insulators, semiconductors and metals [20].*

2.1.2 Bolometer

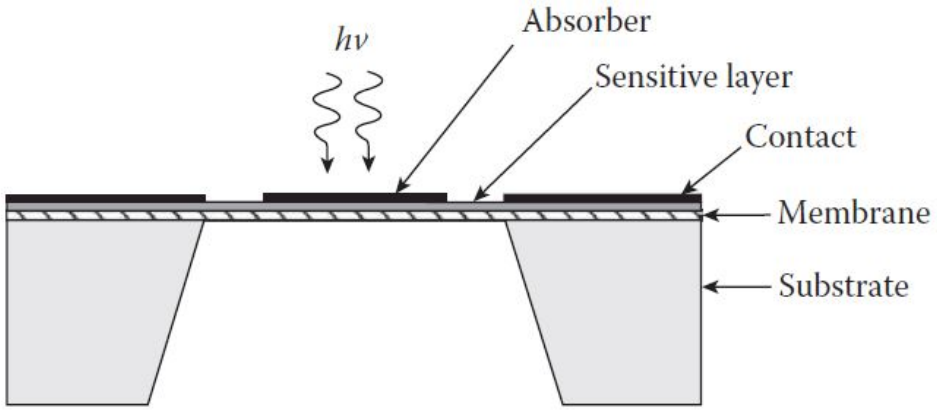

Figure 2.6: *Schematic of thin-film bolometer [3].*

Unlike the thermopile, the bolometer's sensing scheme relies on the change in electric resistance of the material when exposing to thermal radiation. For instance, when a

conductive material receives thermal radiation, the electrical resistance of the material increases as temperature is increased. Thus, in this case, the temperature coefficient of resistance (TCR) is an important parameter and can be expressed as:

$$TCR = \frac{1}{R}\frac{dR}{dT}, \tag{2.2}$$

where R is the electrical resistance of the absorber material and T is the temperature of the absorber. A lager TCR produces a larger voltage readout ΔV according to:

$$\Delta V = IR\Delta T \cdot \text{TCR}, \tag{2.3}$$

where I is the bias current supplying to the readout circuit. Due to this specific sensing mechanism (i.e., resistance changes with temperature), a constant bias current has to be supplied to the bolometer circuit, in order to generate a reliable voltage readout. Since the bias current is maintained in a fixed value, the change in resistance due to thermoelectric effect can be directly associated with the readout.

2.1.2.1 Metal bolometer

The oldest type of bolometer uses metal as its absorber. Due to the relatively large thermal capacity of metal, in order to optimize the thermal time constant, the absorber made of metal is always a thin-film, and most commonly fabricated by a metal evaporation process. For most of the metals, TCR is typically around 0.3%/K which is on average ten times smaller than semiconductors such as silicon; leading to low sensing performances (e.g., lower detectivity and responsivity). Platinum (Pt) film is widely used in conventional metal bolometers given its good mechanical properties in thin-film form, good chemical stability, and well-investigated optical properties and TCR. The highest documented value of TCR for the thin-film Pt is 0.15%/K [21] which is low compared with other thin-film metals. However, Pt film's properties are highly predictable which

make them easy to calibrate.

Another special candidate attracted many attentions in the late 90s is titanium. Despite its slightly lower TCR (0.25% [22]) at room temperature, its high thermal resistance R_{th} provides the desire thermal isolation and further leads to high responsivity.

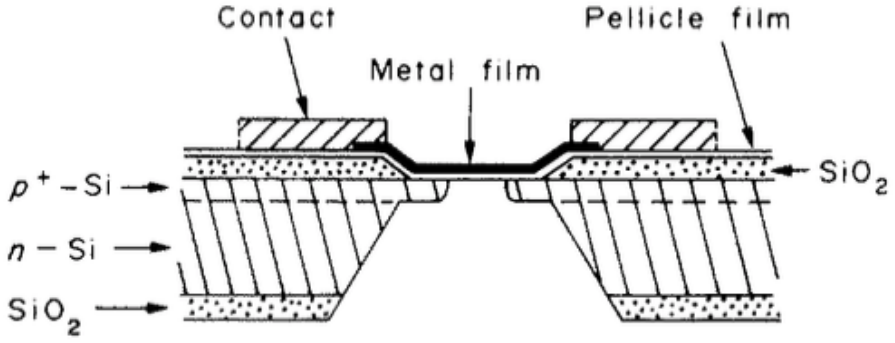

Figure 2.7: *Metal film bolometer detector [23].*

The design of the conventional metal bolometer is generally centred on thermal aspects. In general, the sensing element (i.e., metal absorber), the electrical contact and the substrate are the main subsections of a metal-film bolometer as shown in Fig. (2.7). During the fabrication process, the metal film and the pellicle film are first deposited on the front surface of the silicon wafer. Then the back side of the wafer undergoes multiple steps of an-isotropic etching which removes the majority part of the silicon. The purpose of deposing a pellicle film between the metal and the silicon wafer substrate is to provide better thermal isolation and further improve the performance of the bolometer. If the metal film is directly in contact with the silicon wafer substrate, the large substrate contributes to total thermal capacitance. Hence the thermal response of such bolometer will be drastically slower.

Beside from the design perspectives of the sensing element itself, the packaging for the bolometers has also been analyzed carefully [21]. To minimize heat transfer via solid-state conduction and convection, a few types of low conductivity gases have been used to fill the encapsulation of the sensing element, such as Xe and Freon-22. In brief, these types of

low conductivity gases double the responsivity of the bolometer when the encapsulation is above 100 torr [see Fig. (2.8)]. Note that the responsivity of the bolometer is enhanced drastically by vacuum packaging [24]. The responsivity here is expressed in the form [21]:

$$\Re = \frac{\epsilon \cdot B \cdot I \cdot R \cdot \mathrm{TCR}}{G \cdot (1 + 4\pi^2 f^2 \tau^2)^{1/2}}, \tag{2.4}$$

where ϵ is the emissivity of the absorber, $B = R_L/(R + R_L)$ is the readout circuit bridge factor, R_L is the series load resistance, G is the thermal conductance of the bolometer to the environment by solid-state conduction, f is the frequency of signal modulation and τ is the thermal time constant.

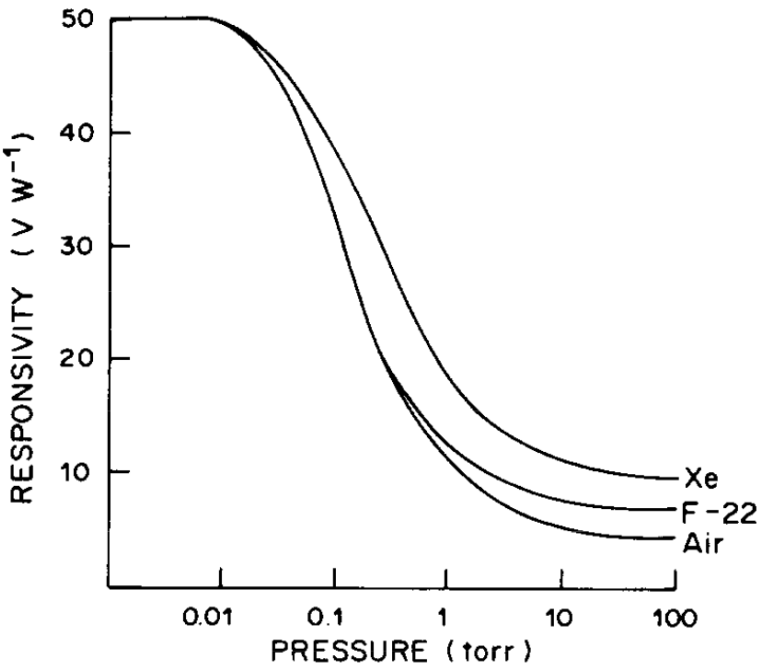

Figure 2.8: *Responsivity of metal-film bolometer as a function of pressure in different gases.[21]*

2.1.2.2 Semiconductor bolometer

In the more recent history of bolometer, semiconductor plays an important role due to its high TCR and highly developed fabrication process. The TCR of a semiconductor can be up to -7%/K [25] which in an order of magnitude larger than any metal material. This

TCR can be easily controlled by the doping level of the material and also the deposition condition. Here we are looking at a few different design iterations in Fig. (2.9), these designs all consist both metal and semiconductor. The semiconductor can be regarded as an optical cavity which can be tuned to reach maximum absorption. The top metal serves as an anti-reflector which helps the semiconductor cavity to absorb more infrared. Whereas the bottom metal film acts both as a back reflector and providing electrical contact, which the resistance value of the semiconductor can be measured by an external readout circuit. Note that in the "gap" design [see Fig. 2.9(a)], due to the existence of the insulator, only the semiconductor locates in the "gap" region is used as the resistance for monitoring temperature variation.

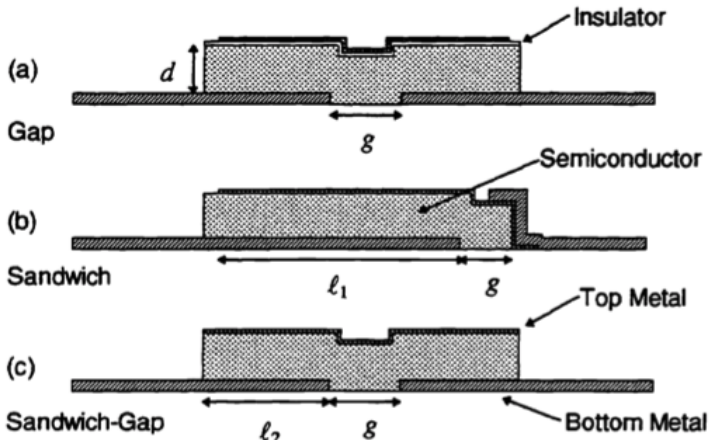

Figure 2.9: *Three different designs of the semiconductor thin-film bolometer.[26]*

The most popular type of the sensing element in semiconductor bolometers is made by combining vanadium oxide (VO_2) and Si_3N_4 together; in specific, the VO_2 oxides are sputtered on top of a Si_3N_4 microbridge substrate. The main advantage of VO_2 is its ability of reaching high TCR with very low resistance at room temperature [see Fig. (2.10)]. This characteristic drastically lowers the electric Johnson noise of the bolometer. However, note that the vast majority of the existing bolometer are Johnson noise limited (i.e., still very far away from reach the fundamental detectivity limit of thermal detector).

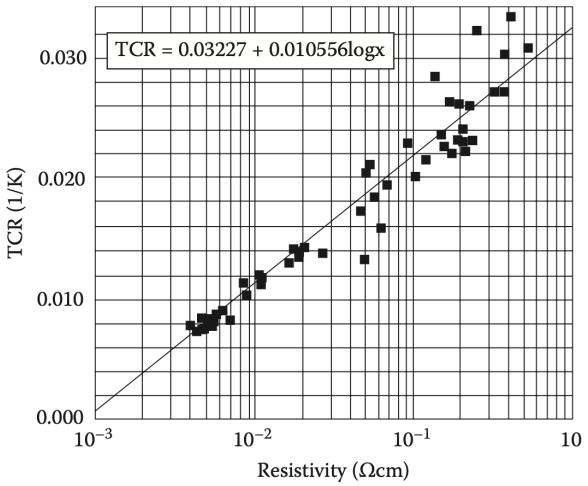

Figure 2.10: *Temperature coefficient of resistance versus resistivity for thin films of mixed vanadium oxides.[3]*

2.2 Mechanical resonator-based bolometers

As we discussed in the previous sections, thermopiles and traditional bolometers all rely on the change in electrical effect of metals and semiconductors. This traditional sensing mechanism induces a performance trade-off which limits the detectivity of the traditional bolometers (i.e., Johnson noise limited). More recently, efforts have been devoted to addressing this issue by replacing the electric sensing scheme with resonant sensing which measures the infrared by the shifts in mechanical resonance of a thin-film material. As the sensing element (i.e., thin-film semiconductors) absorbs the thermal radiation, the internal stress of the material changes, which then alters the mechanical resonance. This detection of the shifts in mechanical resonance can be either detected by an optical (e.g., laser interferometer) or an electrical (e.g., piezoelectric effect) readout methods. The mechanical resonator-based bolometers have shown bright prospect in the field of thermal radiation sensing.

2.2.1 Torsional resonator

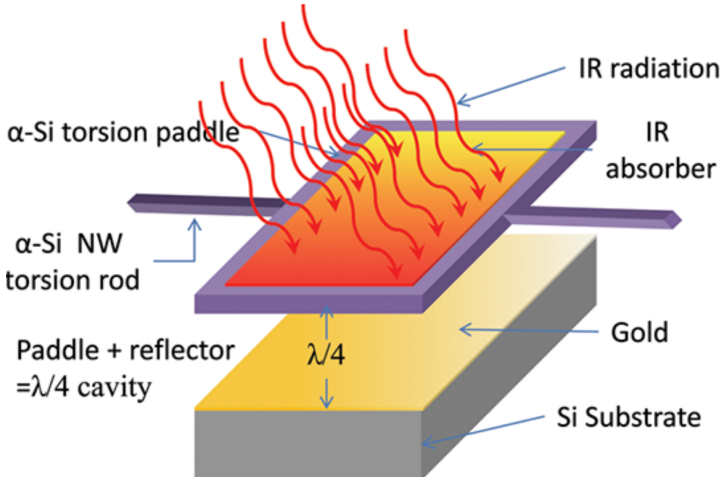

Figure 2.11: *Schematic of layout of a torsional-frequency-shift-based IR detector.[4]*

The nanomechanical torsional resonator [4] is one of the most important foundational work of the resonator-based bolometers that use the resonant sensing scheme for detecting thermal radiation. As it is shown in Fig. (2.11), the torsional resonator has two nano scale (100×100 nm^2 cross sectional area) amorphous silicon (α-Si) torsional rods that provide mechanical support and ensure great thermal isolation [≈ 0.1 W/(m $\cdot$ K) reported thermal conductivity] for the sensing element due to its ultra-narrow geometry. The material of the absorber is selected to be a low-stress SiN membrane, due to its temperature-sensitive internal stress and low mechanical damping (high mechanical Q-factor). The whole device sits on top of a piezoelectric disk which actuates the rotational motion of the absorbing panel. The mechanical displacement of the panel is measured by an external laser interferometer setup. The silicon substrate, beneath the absorbing panel, is gold coated. This coated substrate and the panel form an optical cavity which boosts the absorption of the sensing element since all the transmitted infrared will be reflected back to the absorbing panel for the second chance of absorption. This resonator has two different modes of vibration: torsional mode and flexural mode. The flexural mode is proved to have a slightly higher mechanical Q-factor, whereas the torsional mode

exhibits a far superior dynamic range (DR). Here, DR means the logarithmic ratio between the device noise floor and the maximum level of the actuated amplitude until the mechanical non-linearity is observed.

2.2.2 Doubly clamped beam resonator

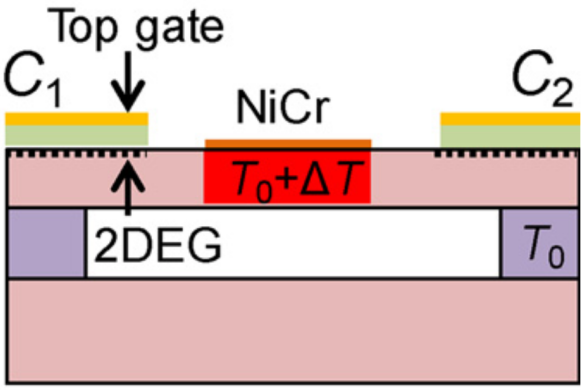

Figure 2.12: *Schematic of layout of a doubly clamped beam resonator.[5]*

The doubly clamped beam resonator (length: 120 μm, width: 30 μm) [5] also utilizes the resonant sensing scheme. Fig. (2.12) shows the cross-sectional schematic of the beam resonator. The NiCr bridge acts as the vibrating part of the beam resonator which both ends are clamped by the top gates and the 2DEG layer. The 2DEG layer consists of a undoped $Al_{0.3}Ga_{0.7}As$ spacer layer and a GaAs capping layer. The major difference between this particular resonator and the previous torsional resonator [2.2.1] is that this design uses the piezoelectric effect for both actuation and detection (i.e., $C1$ is actuating, $C2$ is detecting). This simultaneous electrical drive and detection make this detector convenient to integrate with other electronics such as complementary metal-oxide-semiconductor circuit (CMOS). Despite the noise equivalent power (NEP) of this particular design being slightly worse than the torsional resonator, its specific detectivity (3×10^8 cmHz$^{1/2}$W^{-1}) is still better than the best thermistor bolometer showed in Fig.(2.1).

2.2.3 H-shape torsional resonator

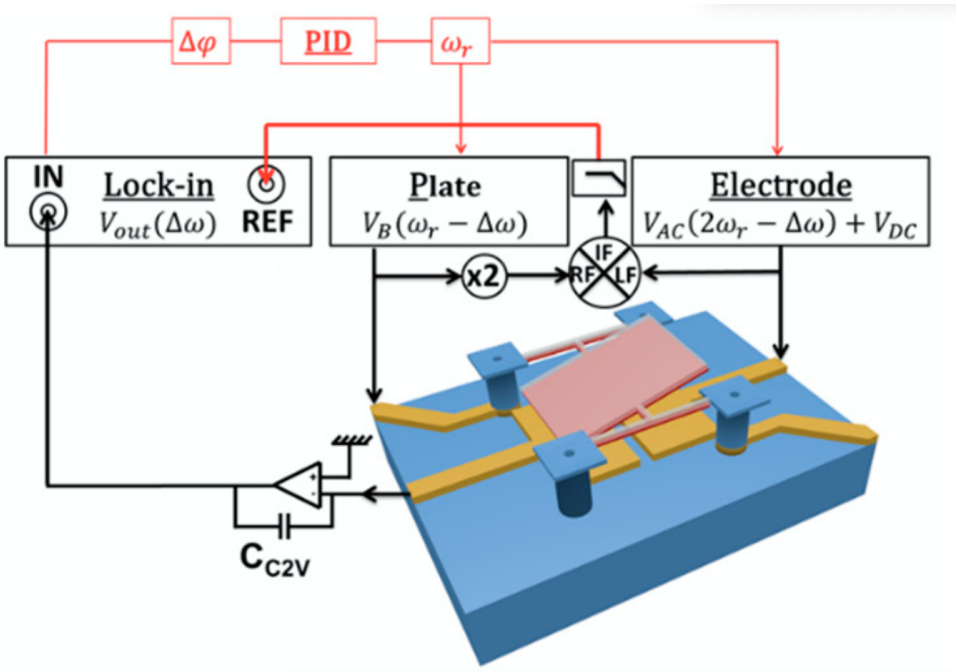

Figure 2.13: *Schematic of the set-up for characterizing the pixels in a down-mixed readout scheme (in open loop or in a closed-loop: red part).[27]*

The H-shape torsional resonator IR detector [27] is inspired by the previously discussed torsional resonator (2.2.1) with improvement in many aspects. This design achieves a 20 mK temperature sensitivity which exhibits an order of magnitude better performance than the original torsional design (390 mK) [4]. As shown in Fig. (2.13), the surface of the absorbing panel and the bridge are coated with VO_x to increase its temperature sensitivity. There are several metallic electrodes located underneath the absorbing panel, which are for electrostatic actuation and capacitive measurement. The actuation and the measurement form a closed-loop system for the resonator to vibrate at its instantaneous frequency according to the temperature change. This closed-loop system produces a very well-defined and sharp mechanical resonance.

2.2.4 Graphene resonator

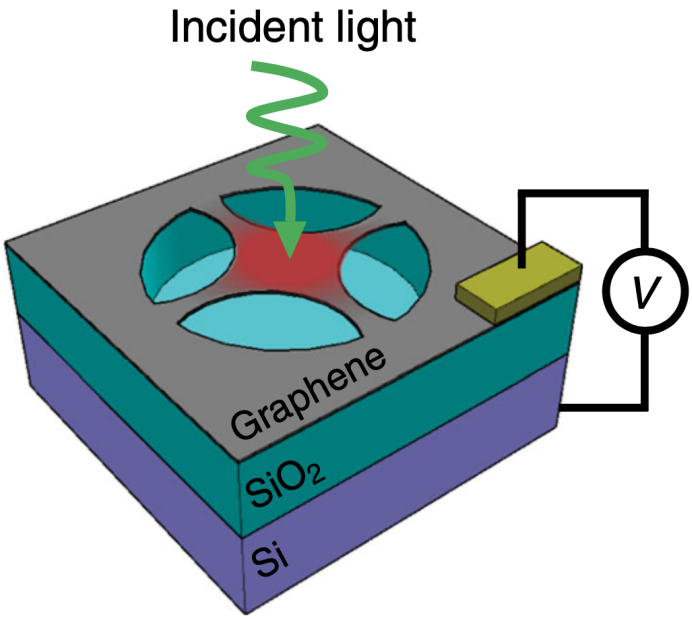

Figure 2.14: *Illustration of the graphene bolometric detection scheme.[6]*

Recently, graphene attracts many interests in different fields. The graphene resonator [28] shown in Fig. (2.14) utilizes a trampoline-shape graphene membrane that is suspended on a silicon substrate and then cut by a focused ion beam. The trampoline shape enhances the thermal isolation of the absorbing panel by leaving four narrow heat channels. Similar to the torsional resonator in the previous Section (2.2.1), this resonator has an optical readout and is actuated by supplying an AC voltage between the membrane and the substrate. Due to the optical readout, the noise equivalent power (NEP) of this specific design can be 2 pWHz$^{(-1/2)}$, which is the lowest out of all the previous designs. Graphene membrane mechanical resonance is not as temperature sensitive as other types of low stress membranes (e.g., low-stress SiN), but it possesses extreme thermal stability over a large temperature range.

2.2.5 SiN resonator

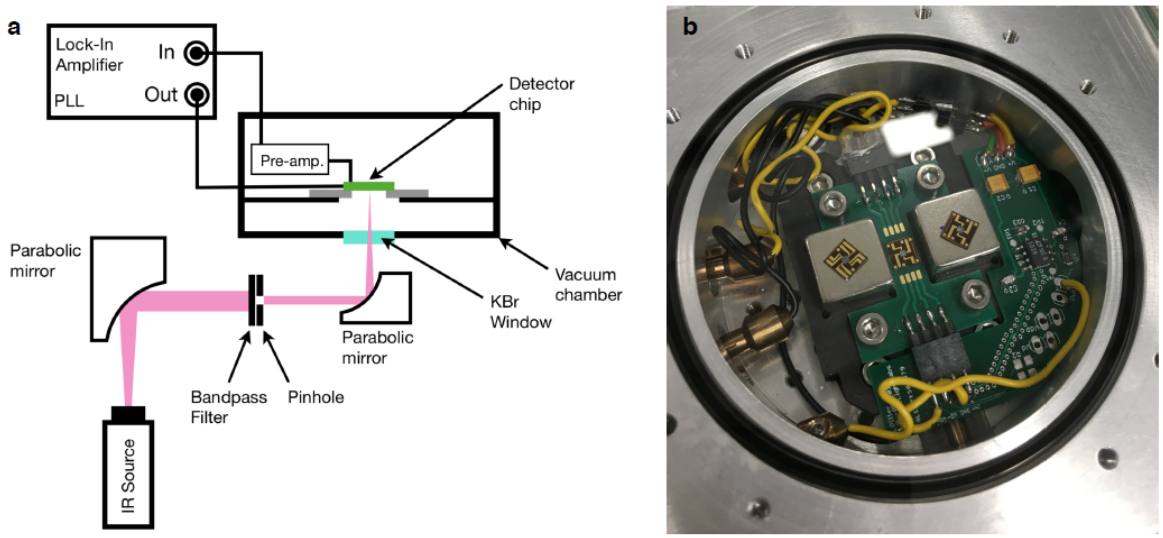

Figure 2.15: *(a) Schematic drawing of the experimental setup. (b) Photograph of the detector chip sitting in-between two magnets inside a vacuum chamber.[15]*

Fig. 2.15(a) shows the schematic layout of a SiN drum-head resonator-based bolometer setup [15], which uses a 50 nm thick SiN drum resonator as the infrared absorber. The bandpass filter is located between the IR source and the SiN resonator to ensure an optimum infrared absorption. Fig. 2.15(b) exhibits the actual setup through the glass view port of a vacuum chamber. This work shows many similarities with our objective design for the radiation sensor which includes a closed-loop drive and resonance tracking using the Phase-Lock Loop (PLL). The SiN membrane is excited inductively by a coated electrode. Even though this design is built with a complete integrated closed-loop driving system, it still shows a non-optimum performance and far from reaching the fundamental detectivity limit of the thermal detector due to its membrane dimension. The reported noise equivalent power (NEP) is 320 pW $Hz^{-1/2}$ for a 1×1 mm window size.

2.2.6 Performance comparison

2.2.6.1 Detectivity

Table 2.1: *Comparing important parameters between discussed resonator-based bolometers.*

Comparison between resonator-based bolometers				
Types	D^* ($\mathrm{cmHz^{1/2}W^{-1}}$)	A_d ($\mathrm{cm^2}$)	Q-factor	NEP ($\mathrm{W\ Hz^{-1/2}}$)
Torsional Resonator (2.2.1[4])	$< 2.2 \times 10^8$	$\approx 1 \times 10^{-7}$	≈ 1555	$< 1.44 \times 10^{-12}$
Doubly Clamped Beam Resonator (2.2.2[5])	$\approx 3 \times 10^8$	$\approx 3.6 \times 10^{-5}$	≈ 3000	$\approx 2 \times 10^{-11}$
H-shape Torsional Resonator (2.2.3[27])	$\approx 2.2 \times 10^8$	$\approx 4.4 \times 10^{-7}$	≈ 1800	$\approx 1.44 \times 10^{-12}$
Graphene Resonator (2.2.4[6])	$\approx 1.3 \times 10^8$	$\approx 1.2 \times 10^{-7}$	≈ 900	$\approx 2.66 \times 10^{-12}$
SiN Resonator (2.2.5[15])	$\approx 3.125 \times 10^8$	$\approx 1 \times 10^{-2}$		320×10^{-12}
Fundamental Limit [3]	$\approx 1.8 \times 10^{10}$			

The most universal parameter used for assessing the performance of bolometers is specific detectivity ($D^* = \sqrt{A}/\mathrm{NEP}$) [1]; which is the reciprocal of noise equivalent power (NEP), normalized by the absorber dimension. Note that NEP is the input signal power that makes the noise-to-signal ratio of one. A bolometer with a higher D^* can detect smaller temperature difference. In Table (2.1), D^* of all four previously discussed resonator-based bolometers are presented. Some of them indeed show better performance than the traditional bolometers, such as the doubly clamped beam resonator [5] which achieves a D^* as high as 3×10^8 $\mathrm{cmHz^{1/2}W^{-1}}$. However, they are all far away from reaching the fundamental limit of the ideal thermal detector, which is reached when the only noise source is thermal coupling noise caused by pure radiative heat exchange with the environment. In other words, the total thermal conductance G between the absorber

and the environment is equal to the radiative thermal conductance (in watts per kelvin) $G_{rad} = 4A\sigma\epsilon T_{\infty}^{3}$ [3], where σ is the Stefan-Boltzmann constant. It should be noticed that the expression of G_{rad} here is derived by assuming small temperature difference between the absorber and the environment which is true for the scenario of thermal radiation sensing [See Section (4.1.1) for detailed derivations of G_{rad}].

2.2.6.2 Figure of merit (FOM)

Besides from specific detectivity (D^*), another frequently encountered metric for evaluating bolometer performance is the figure of merit (FOM = NETD $\times$ τ_{th} $\times$ A_d) [29]; where NETD is the noise equivalent temperature difference, τ_{th} is the thermal time constant and A_d is the area of the bolometer absorber. Here, NETD can be considered as the resolution of the device which indicates the minimum temperature difference that a bolometer can measure and τ_{th} indicate the speed of a bolometer. In other words, a smaller FOM indicates a better bolometer overall (i.e., detect smaller temperature difference and faster response). Note that the FOM metric not only takes the resolution (i.e., NETD or NEP) of the device into the consideration, it also includes the speed (i.e., τ_{th}) of the device in the equation. This makes the FOM metric a more comprehensive evaluation due to the fact that bolometers can sacrifice their speed for a better detectivity but a high-performance bolometer is required to achieve both. Through the literature review, the H-shape torsional resonator (2.2.3)[27] uses this particular metric for comparing its performance with other similar types of bolometers [30, 31, 32, 33] which also utilize the torsional mechanism of the resonator and the comparison shows that the H-shape torsional resonator (2.2.3)[27] achieves the minimum FOM, hence a overall better performance when considering FOM as the evaluation matrix.

2.2.7 Heat transfer analysis in mechanical resonator-based bolometers

As discussed previously, achieving radiation-dominated thermal coupling is the key requirement for reaching the fundamental detectivity limit of the thermal detector. However, according to the literature reviews in Section (2.2) of the five most up-to-date mechanical resonator-based bolometers [4, 5, 6, 15, 27], none of these works provides a comprehensive closed-form analysis for the thermal coupling conditions of their bolometers. Instead, some of them [4, 27] provide finite-element simulations for the temperature profiles of their absorbers when exposing to thermal radiation. Others [5, 6, 15] use overly simplified analytical models (i.e., solely considering heat being dissipated from the heated absorber by solid-state conduction) to predict the temperature of the heated absorbers which completely ignore the effect of thermal radiative exchange between the absorber and the environment.

3. Experimental methods

3.1 Overall considerations of the experimental setup

The experimental part of this work includes actuating the mechanical resonance of the SiN membrane and recording its resonance shift when the membrane is exposing to an external radiative heat source. One of the major requirements for the SiN membrane to vibrate at a high mechanical Q-factor resonance is a high-vacuum environment. The vacuum environment prevents the vibration of the membrane from being damped by the surrounding air (i.e., lowering Q-factor) and also helps to suppress the unwanted convective heat transfer between the membrane and the environment.

To actuate the mechanical resonance of the membrane, we glue a small portion of the membrane supporting frame corner to the edge of a clean microscope glass-slide, with a piezoelectric actuator glued on its other end of the glass slide for performing the external actuation as shown in Fig.(3.1). The front side of the SiN membrane is shielded by a custom made aluminum reflector with a circular window to prevent the silicon frame supporting the membrane from heating up and affecting the result of the experiment. This glass-slide (i.e., contains the SiN membrane, the aluminum shield and the piezo-actuator) is then glued to an optical positioning stage in a high vacuum chamber. An optical fiber tip points perpendicular to the back side of the SiN membrane to detect the mechanical movement of the membrane. A ceramic heater is located on the front side of the membrane to radiatively heat up the membrane during the experiment [see Fig.(3.3)]. Detailed drawings of the front and top view with dimensions of this glass slide setup are provided in Fig. (3.2).

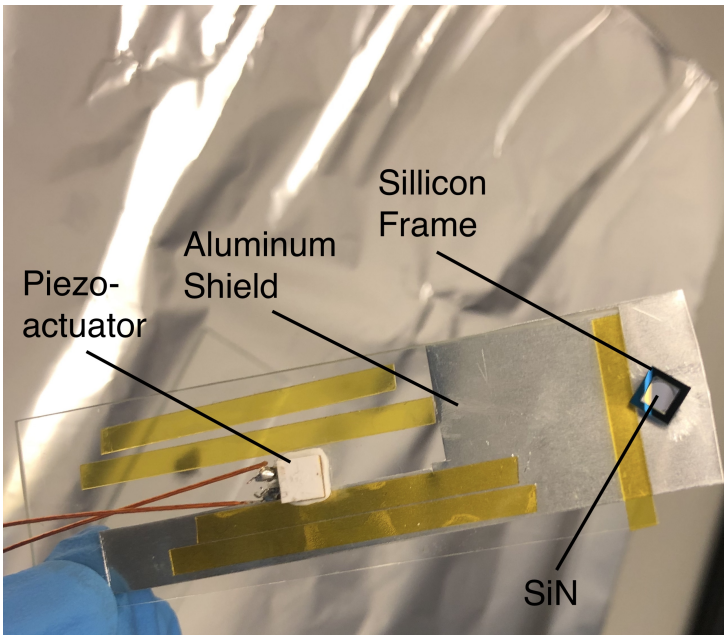

Figure 3.1: *Photograph of the glass slide with SiN membrane, piezo-actuator and aluminum shield.*

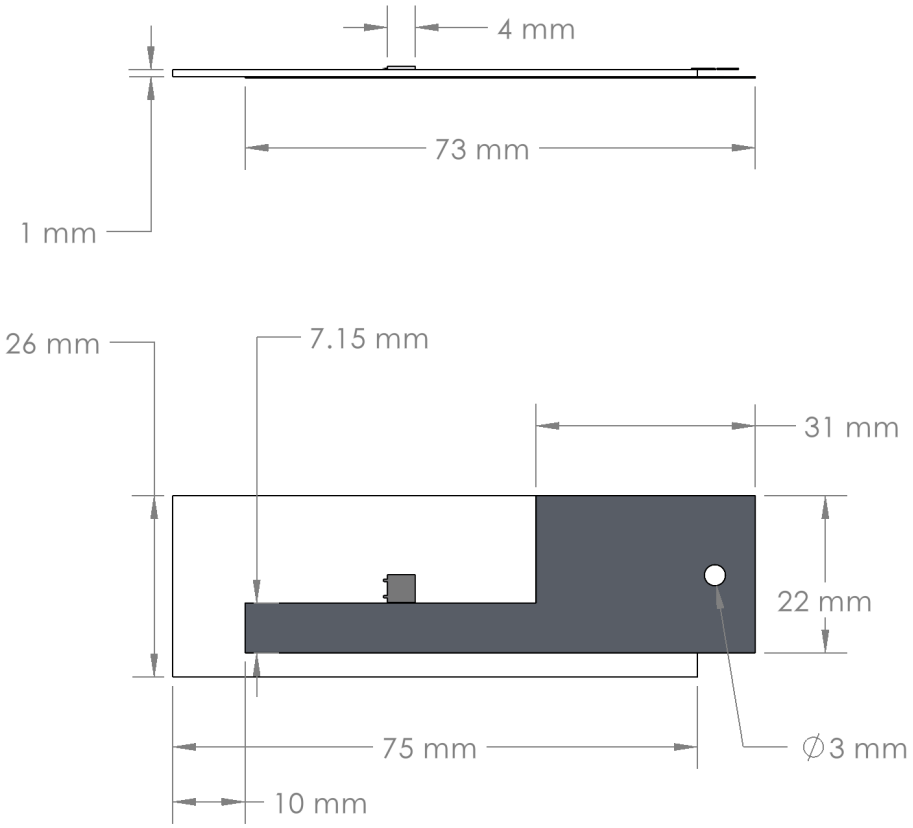

Figure 3.2: *Detailed dimensions and CAD drawing of the glass slide setup.*

3.2 Laser interferometer

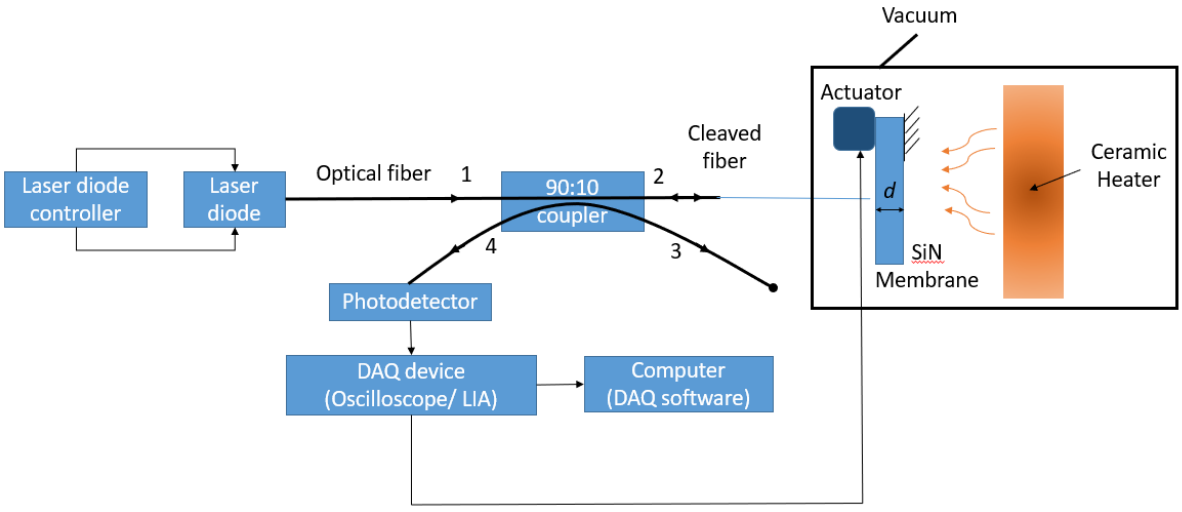

Figure 3.3: *Illustration of the fiber-optic interferometer. (LIA stands for lock-in amplifier)*

Laser interferometers are commonly used for detecting extreme small-scale displacement of objects. Here, we use a conventional fiber-optic interferometer [34] to detect the displacement of the membrane surface during vibration. This interferometer [Fig. (3.3)] consists of single-mode optical fibers, an optical coupler, a photodetector and a laser with constant wavelength. In our specific setup, we use a 90:10 coupler which means 90% of the light from the laser is wasted and the rest of the light hits the SiN membrane then reflects back to the photodetector. Other common types of coupler such as 50:50 coupler can also be used in this interferometer setup as long as there is enough amount of light that can be detected by the photodetector. Note that the whole interferometer is positioned outside of the high-vacuum environment and only the cleaved fiber tip is inside the vacuum chamber to maintain a close distance with the surface of the SiN membrane.

The mechanism that allows the laser interferometer to detect displacement is the wave interference effect. A cleaved optical fiber tip reflects back roughly 4 % of the light (i.e., at the glass-air interface) that is going out and this 4% of the light will reach the

photodetector on the other side of the optical coupler. When the object (SiN membrane) is positioned in a close distance to the fiber tip, the light coming out of the fiber, hits the surface of the object and part of the light also reflects back to the photodetector. Thus, these two light beams (i.e., reflected from the fiber tip and object) create an interference pattern that can be correlated to the membrane position in real-time. The voltage signal coming out of the photodetector therefore varies according to this interference effect. In fact, the relation between the distance and the signal amplitude can be represented by Eq. (3.1) [34] and Fig. (3.4):

$$V = V_{mid} + Acos(\frac{4\pi d}{\lambda}), \tag{3.1}$$

where V is the signal amplitude, V_{mid} is $(V_{max} - V_{min})/2$, d is the distance between the object and the fiber tip, and λ is the laser wavelength (1550 nm in our case). We can further take derivative of V with respect to small variations of d, when the optical fiber is positioned at the point of maximum slope in Fig. (3.4):

$$\Delta d = \frac{\lambda \Delta V}{2\pi(V_{max} - V_{min})}. \tag{3.2}$$

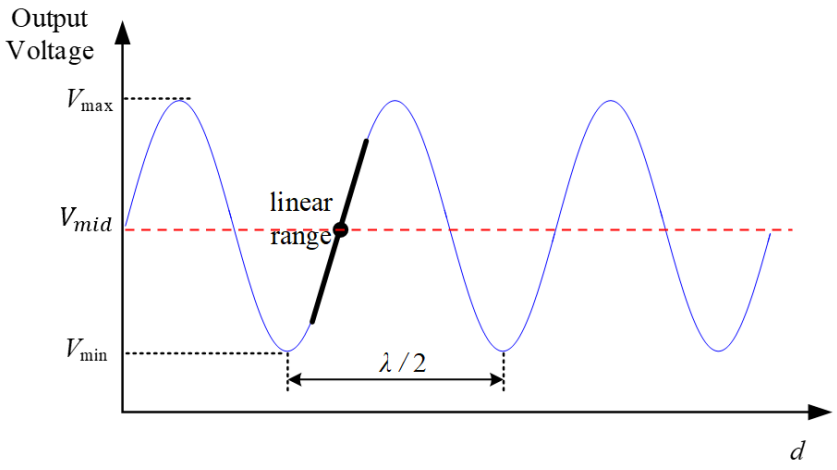

Figure 3.4: *Sinusoidal relation between the distance and the signal level.*

Note that a larger fringe (i.e., $V_{max} - V_{min}$) represents a stronger signal. Before the

measurement takes place, not only we need to make sure the fringe is as large as possible (i.e., large signal), we also need to "park" the distance right at the middle of the linear region [see Fig. (3.4)] to utilize the full range of the linear region. We also measure V_{max} and V_{min} by displacing the optical fiber, such that we can later convert the voltage signal (ΔV) to actual displacement (Δd) using Eq. (3.2).

3.3 Custom vacuum chamber

As it is indicated in Fig. (3.3), the SiN membrane is positioned inside of a custom high-vacuum chamber to suppress the air damping and convective heat transfer. This vacuum chamber [see Fig. (3.5)] is manufactured by Kurt J. Lesker [35], then assembled and tested by one of our colleagues [36]. The high-vacuum chamber reaches 1E-5 Torr after one hour of pumping down and the minimum pressure (1E-6 Torr) can be reached after 100 hours of operation. The glass slide which the actuator and the membrane are attached to is mounted on an optical stage (stage-A) using a vacuum compatible double-sided tape. The optical fiber is attached to the other optical stage (stage-B), ensuring that the fiber tip and the membrane surface are perpendicular to each other for maximizing reflection signal. The position of both stages can be adjusted by three precise linear piezoelectric actuators (8302-V) from Newport. Note that stage-A only has one degree of freedom (i.e., up and down), whereas the stage-B has two degrees of freedom (i.e., back and forth, left and right). With this particular setup, we can precisely control the distance between the fiber tip and the membrane, also the precise location of the fiber tip is pointing at. The ceramic heater is mounted on an optical post which is located in a short distance with the membrane. Note that this heater is controlled by a power source outside of the chamber. The chamber pressure is monitored by a pressure gauge which connects to the pump continuously during the experiment. All the equipment inside of the chamber is made of vacuum compatible materials (e.g., high density metal) for maintaining a stable pressure level.

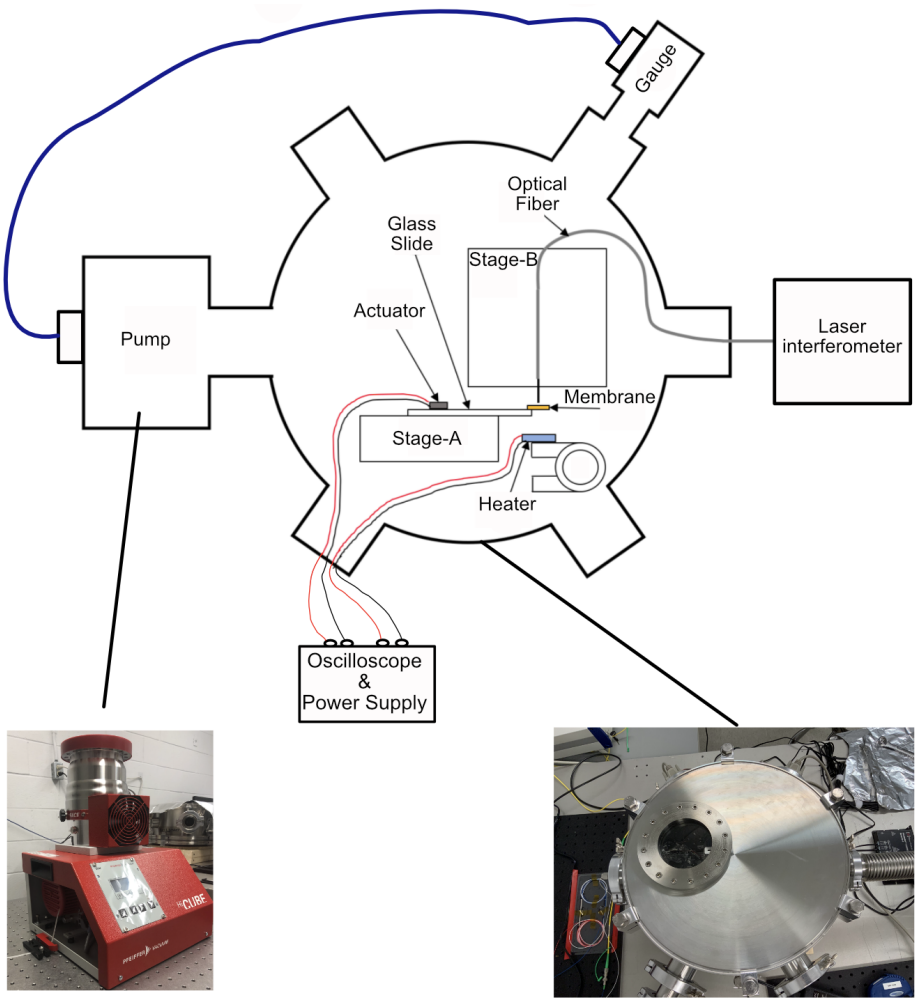

Figure 3.5: *Schematic of the high-vacuum chamber setup.*

3.4 Tracking the resonance

3.4.1 Mechanical modes of vibration

There are many spatial vibration modes of thin-film membrane resonator which are denoted by tensor notation conventionally. For instance, a mode (m, n) represents a vibration mode which has m number of antinodes in x direction and n number of antinodes in y direction, as illustrated in Fig. (3.6). Note that the antinode represents the location of maximum amplitude of a vibrating membrane. As the resonance frequency increases, the number of antinodes on the vibrating membrane increases simultaneously. This rela-

tion between the number of antinodes and the resonance frequency can be described as Eq. (3.3) [9]:

$$f_{m,n} = \sqrt{\frac{\sigma_0(m^2+n^2)}{4\rho l^2}}, \tag{3.3}$$

where σ_0 is the tensile stress of the membrane, ρ is the material density and l is the side length of the square membrane. Hence, to actuate a higher order mode (i.e., higher value in m and n), the actuation device is required to operate at a higher frequency.

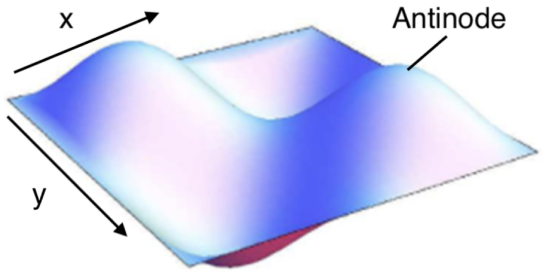

Figure 3.6: *Schematic of mechanical mode (2,2), taken from [9].*

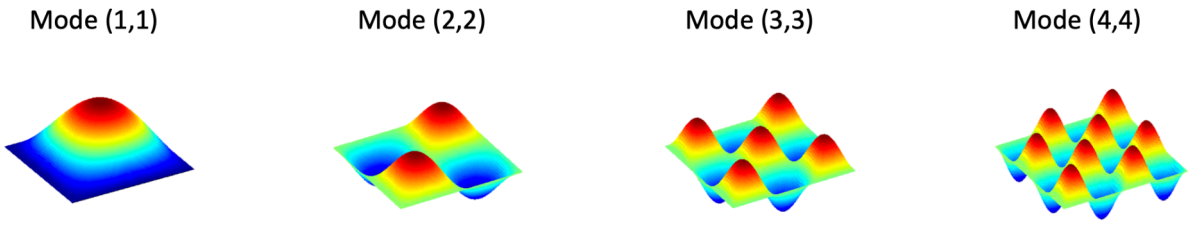

Figure 3.7: *Schematic of symmetric mechanical modes, taken from [36].*

For the purpose of resonant sensing (i.e., tracking resonance shift), choosing the right mechanical mode to track is the essential step for initiating a good sensing performance. A suitable mechanical mode possesses a high Q-factor (i.e., extremely under damped), because a high Q-factor mode produces a well-defined resonance (e.g., narrow linewidth) with a high resonance that is easy to track as it shifts. In addition to this, a selected mode has to be located relatively far away from its adjacent mode on the spectrum such that during the resonance shift, the selected mode will not be lost due to overlapping

with its neighbours. The mechanical Q-factor of a specific mode can be computed by Eq. (3.4):

$$Q_{m,n} = \pi f_{m,n} \tau \tag{3.4}$$

where $f_{m,n}$ is the corresponding frequency of mode (m, n) and τ is the time constant during mechanical ring-down [see Fig. (3.8)]. Usually, for higher order mode regime, we enter a "forest of resonance" (i.e., many modes are at close neighboring frequency) which means all the modes are extremely close to their neighbour on the spectrum. Therefore, for the purpose of resonant sensing, choosing a high order mode is not recommended. Note that the non-degenerate modes [see Fig.(3.7)] (i.e., m and n are the same) usually produce higher Q-factor due to geometric symmetry which is suitable for the practice of resonant sensing. In this work, we choose the symmetric mechanical mode (2,2) for these reasons.

3.4.2 Mechanical ringdown

Traditionally, the Q-factor of a resonance can be directly obtained by measuring its linewidth in the frequency domain. However, a resonance with a high Q-factor exhibits an extreme narrow bandwidth which is too narrow to measure. Hence, it is required to perform a mechanical ringdown for such measurement. To begin with, the resonator is excited at its resonance to a certain amplitude which is well above the instrument noise floor. Once the resonance is excited stably, we interrupt the excitation and let the amplitude slowly decrease as it is illustrated in Fig. (3.8). A high Q-factor resonance usually experiences a fairly long ringdown time (e.g., for a mode 2,2 resonance of one million Q-factor, the ringdown time is $\approx$ 10 s) as an indication of the extreme under-damped vibration.

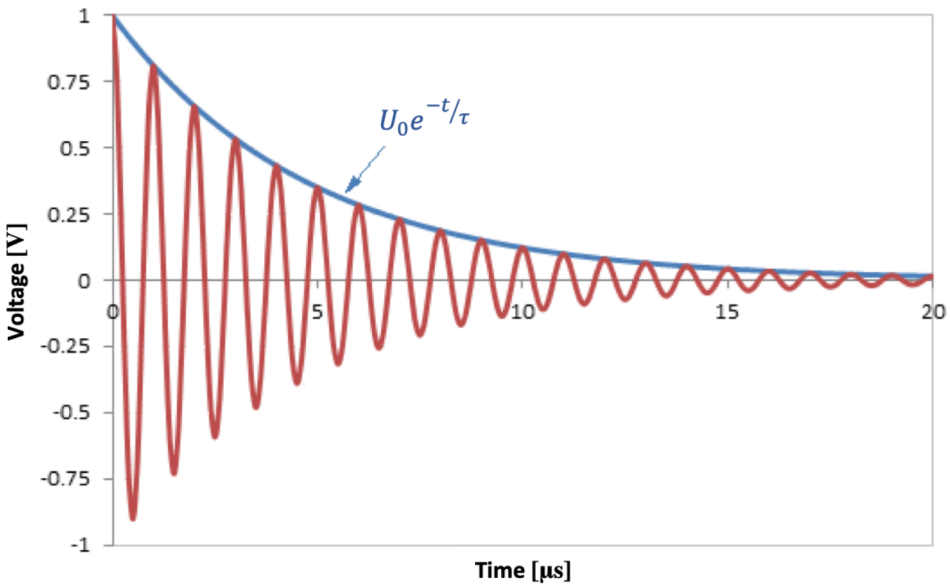

Figure 3.8: *Schematic of mechanical ringdown signal and exponential fitting.[37]*

After the real-time amplitude signal of the vibration is recorded, we then fit a exponential decay function to the trace of amplitude over time to extract the time constant τ. By plugging τ back to the Eq. (3.4), we obtain the Q-factor for this particular mode of vibration. As we mentioned before in Section (3.4.1), it is ideal to choose a mechanical mode that has higher Q-factor and also located relatively far away from its neighbour (e.g., non-degenerate modes). Thus, performing a mechanical ringdown is essential for selecting the suitable mechanical mode to track.

3.4.3 Frequency sweeping

Once the suitable mechanical mode of vibration is chosen, we track the frequency shift as its temperature is changed by an external ceramic heater. Since this experiment is still in its preliminary phase, closed-loop control of the excitation has not been implemented yet. Instead, we sweep the excitation frequency within a range repetitively during the experiment to locate the resonance frequency position in frequency domain.

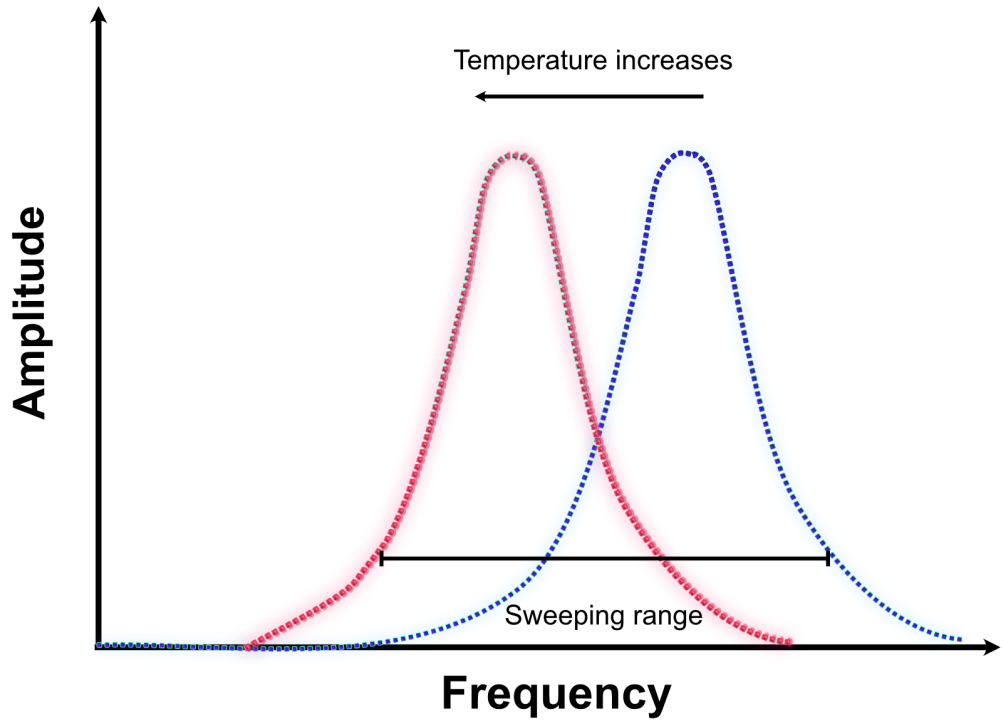

Figure 3.9: *Schematic of the resonance frequency shift during the change of the temperature.*

To perform the data acquisition and the excitation simultaneously, we use a USB oscilloscope [38], developed by Digilent. Inc. This USB oscilloscope is capable of tracking the resonance frequency when the amplitude of the signal is well above the noise floor. During the experiment, due to the change of temperature, the resonance shifts [see Fig. (3.9)]. Thus, to ensure the resonance is always being excited, the excitation signal must be adjusted in real-time. Therefore, we must sweep the excitation frequency such that the resonance can be excited even when it is changing. As a rule of thumb, the sweeping duration time must set to be shorter than the mechanical ringdown time such that before the resonance amplitude dies completely, it can be exited again to a decent level (i.e., can be easily recognized over the noise floor) that can be tracked. To determine the frequency sweeping range, we can approximate the magnitude of the shift before the experiment and set the sweeping range accordingly.

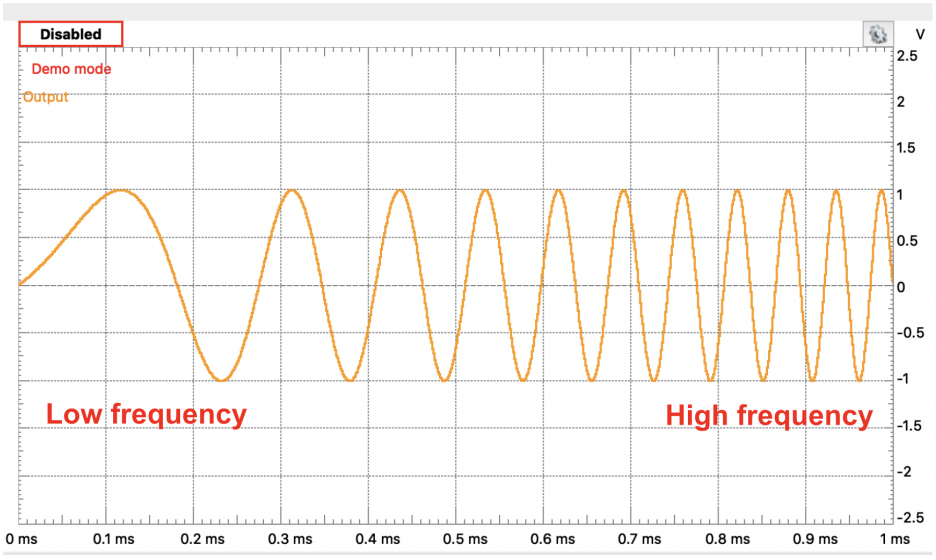

Figure 3.10: *Exaggerated demonstration (i.e., not during the real experiment) of the USB oscilloscope software interface for sweeping frequency output.*

3.5 Shielding the frame

As it is shown in Fig. (3.1), one side of the SiN membrane is shielded by a highly reflective aluminum sheet metal which has a documented reflectance of 85 to 95% [39]. This sheet metal has a drilled hole with a similar size of SiN membrane window which allows the ceramic heater to solely heat up the SiN membrane instead of heating up the silicon frame simultaneously. According to our preliminary experimental results, we find that if the aluminum shield is not in place, the thermal expansion of the silicon frame has a non-negligible effect. Theoretically, as the temperature of SiN membrane increases, the membranes stiffness decreases which causes its mechanical resonance frequency to be lower. However, this frequency shift can be cancelled by the expanding silicon frame when the frame itself also heats up, because an expanding frame stretches the membrane and increases its stiffness. As the result, when we increase the temperature of the heater, the resonance frequency counter-intuitively increases slowly due to the thermal expansion of the silicon frame. With the highly reflective aluminum sheet metal in place, this

undesirable effect can be mitigated. To further minimize the effect of the overheating of the silicon frame, we deliberately keep the time duration of each measurement short (i.e., as soon as the temperature of the heater becomes stable) such that the resonance frequency shift of the membrane is dominantly caused by the membrane thermal response instead of the frame thermal response since the silicon frame has far larger thermal mass and will respond much slower than the membrane.

3.6 Ceramic heater

Prior to initiating the experiment, the metal ceramic heater that is used as a thermal radiation source is characterized. A precise way of monitoring the temperature of the metal ceramic is by tracking its electric resistance. Just like a traditional metal bolometer, this ceramic heater resistance has a linear relationship with its temperature ($R = R_0 + R_0 \cdot \mathrm{TCR} \cdot \Delta T$). The temperature coefficient of resistance (TCR) of this particular heater is found by placing the heater on top of (in contact) a hot plate to conductive increase the temperature, and continuously monitoring the resistance of the heater as shown in Fig. (3.11) [40]. By linearly fitting those data points, the TCR (4.7E-3 K^{-1}) can be obtained.

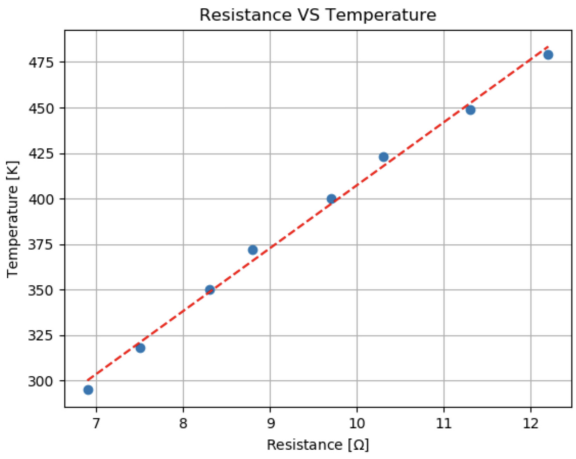

Figure 3.11: *Heater temperature versus resistance, calibrated by putting the heater in contact with a hot plate.[40]*

After obtaining the TCR of the metal ceramic, we apply a voltage to the heater to increase its temperature under high vacuum. The relation between the heater temperature variation and the power supply can finally be experimentally characterized as shown in Fig. (3.12). Thus, during the experiment, the temperature of the ceramic heater is obtained by knowing the electrical power sent to the heater.

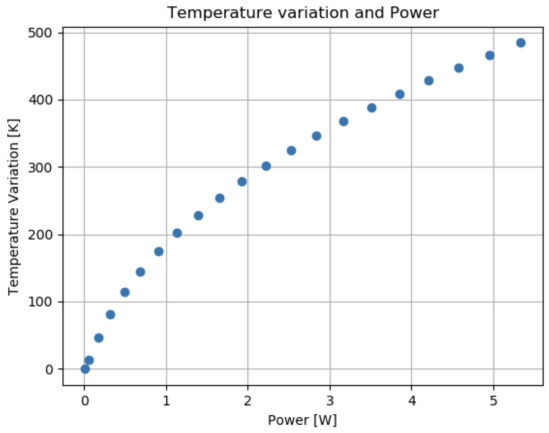

Figure 3.12: *Heater temperature variation versus power inside vacuum.[40]*

4. Results

Even though many resonator-based bolometers [see Section (2.2)] have attempted to break the performance trade-off of traditional bolometers by using resonant sensing instead of the traditional electric sensing scheme, they are still two orders of magnitudes below the fundamental limit [See Table (2.1)]. This discrepancy is in part due to the fact that many existing resonator-based bolometers do not reach radiation-dominated thermal coupling with surrounding environment.

The first step towards achieving a bolometer at the fundamental detectivity limit is therefore to develop a model that quantitatively predicts the thermal coupling between the silicon nitride radiation absorber and its surrounding which is the focus of the follow research article [11]. This article proposes an universal heat transfer model for a thin-film SiN membrane to assess its thermal coupling condition with the surrounding. The following section is the pre-print version [41] of this paper entitled as Radiative Heat Transfer in Free-Standing Silicon Nitride Membranes. This paper primarily provides a two-dimensional closed-form expression of the heat transfer model, in accordance with experimental results. In Section (4.2), we also provide the same model, but in the simple case of an one-dimensional (string) resonator, which is representative of other cases.

4.1 Justifications of major approximations

To establish the heat transfer model for the thin-film SiN membrane, we make several assumptions that are valid for thermal radiation sensing at room temperature. The following sub-sections provide additional details on these assumptions.

4.1.1 Small temperature difference approximation

To obtain a closed-form analytical solution of this radiative heat equation, we must linearize the radiative exchange (G_{rad}) between the membrane and the background environment by assuming a small difference between the temperature of the SiN membrane (T_{SiN}) and the temperature of environment (T_∞). G_{rad} (in watts per kelvin) can then be expressed as a function of radiative power exchange P_{rad} :

$$G_{rad} = \frac{P_{rad}}{T_{SiN} - T_\infty}, \tag{4.1}$$

where

$$P_{rad} = A\sigma\epsilon(T_{SiN}^4 - T_\infty^4). \tag{4.2}$$

By substituting Eq. (4.2) to Eq. (4.1),

$$G_{rad} = A\sigma\epsilon(T_{SiN}^2 + T_\infty^2)(T_{SiN} + T_\infty). \tag{4.3}$$

When assuming small temperature difference, $T_{SiN} \approx T_\infty$, such that Eq. (4.3) reduces to:

$$G_{rad} = 4A\sigma\epsilon T_\infty^3 \tag{4.4}$$

Such an assumption is only valid in the specific case of thermal radiation sensing since the average temperature of the absorber only changes on the order of a few degree kelvins during the measurement [11, 15].

4.1.2 Volumetric heat generation approximation

We model absorbed radiation as a constant heat generation ($\dot{q}$ in W/m^3) inside of the membrane. For this assumption to be valid, the temperature along the direction normal to the surface of the membrane must be uniform. This condition is fulfilled due to the thin-film geometry of the SiN membrane (i.e., thickness on the order of a few hundred nanometers). It should be noticed that such volumetric heat generation approximation is only valid for modeling homogeneous absorption of light everywhere on the membrane. A more complex model would be required for non-uniform absorption conditions.

4.1.3 Dirichlet boundary condition

In the scenario of thermal radiation sensing at room temperature environment, the substrate temperature of the sensing devices (e.g., thermopile and bolometer) should be kept at room temperature stably [1] to minimize thermal noise caused by temperature fluctuation of the substrate. Therefore, we set the boundary condition of the SiN membrane (T_b) to be at room temperature (T_∞).

Another important reason that T_b can be set to T_∞ is that the thermal resistance of the SiN membrane (R_{SiN}) is significantly larger than the thermal resistance of silicon substrate (R_{Si}). We use simple thermal resistance circuit in Fig. (4.1) to demonstrate the solid-state thermal conduction between the SiN membrane and the silicon substrate. Note that T_{max} is the maximum temperature of the SiN membrane.

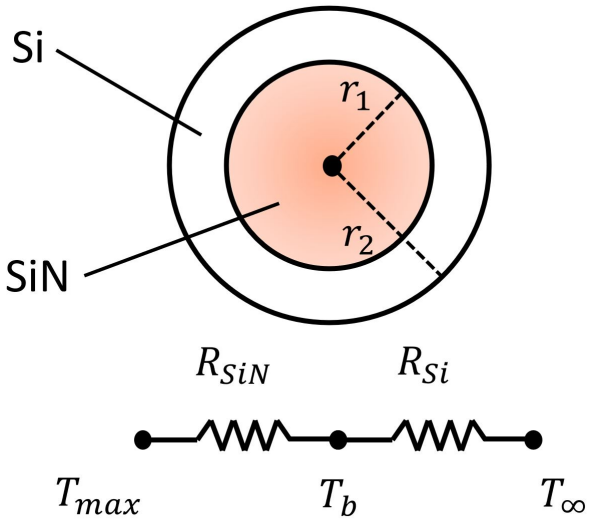

Figure 4.1: *Thermal resistance circuit of a circular SiN membrane for the scenario of a heated SiN membrane conducting heat flux to its silicon substrate via solid-state conduction.*

To obtain T_b, we can treat R_{SiN} and R_{Si} as temperature dividers between T_{max} and T_∞ since the resisters are connected in series:

$$\frac{T_b - T_\infty}{R_{Si}} = \frac{T_{max} - T_\infty}{R_{SiN} + R_{Si}}, \tag{4.5}$$

$$T_b - T_\infty = \frac{T_{max} - T_\infty}{\frac{R_{SiN}}{R_{Si}} + 1}. \tag{4.6}$$

According to Eq. (4.6), when $R_{SiN} >> R_{Si}$, T_b becomes extremely close to T_∞ such that we can set the boundary condition of the SiN membrane at T_∞. It should also be noticed that the thermal conductivity of the thin-film SiN membrane (4 to 10 $\mathrm{W/m \cdot K}$) [42, 43] is at least two orders of magnitude smaller than the silicon substrate (≈ 130 $\mathrm{W/m \cdot K}$) [44] and the thickness of the thin-film SiN membrane (a few hundred nanometers) is at least three orders of magnitude smaller than the silicon substrate (a few hundred microns). This means the magnitude of R_{SiN}/R_{Si} is at least ≈1E5, which results in a negligible temperature difference between T_b and T_∞ referring to Eq. (4.6).

4.2 Pre-print version of the paper

4.2.1 Abstract

Free-standing silicon nitride (SiN) mechanical resonators are of central interests in applications such as temperature and mass sensing, and for fundamental optomechanical research. Understanding thermal coupling between a membrane resonator and its environment is required for predicting thermal noise, frequency noise, as well as sensors responses to temperature changes. In this work, we provide closed-form derivations of intrinsic thermal coupling quantities in free-standing thin films—namely total thermal conductance with the surroundings, thermal response time, and the relative contribution of thermal radiation. Our model is valid for any free-standing thin film anchored on all sides, when considering small temperature differences between the film and its environment. We particularly emphasize the specific case of SiN for which spectral emissivity is thoroughly investigated as a function of thickness and temperature. We find that radiative heat exchanges can play a non-negligible role, and even dominate thermal coupling for membranes of sizes commonly employed in optomechanics experiments. We find that our model is in agreement with preliminary experimental results on radiative heat transfer between a ceramic heater and a 3×3 mm membrane in high vacuum.

4.2.2 Introduction

Thin-film silicon nitride (SiN) membranes are heavily used as mechanical and optical resonators in both fundamental opto-mechanical studies [45, 46, 10] and many state-of-the-art sensing technologies, including ultra-sensitive mass sensing [12], gas detection [47], nanoparticulate mass detection [13], thermal radiation sensing [4, 48, 15, 5] and pressure sensing [49]. Many of these works involve cooling [45, 10], while in other cases, the temperature dependence of membrane stress is used as a sensing mechanism [48, 4, 15, 5], or an active technique for controlling resonator frequency [17].

As such, understanding thermal coupling between SiN membranes and their environment is of central importance. For example, values of thermal conductance (G in W/K) with the environment, and of membrane thermal response time (τ) are central in the calculation of noise processes such as temperature fluctuation noise and temperature-induced frequency fluctuation [50, 51, 52].

Likewise, in the context of nanomechanical radiation sensors [4], understanding the ratio of heat transfer occurring via radiation (x_{rad}) is key for determining ultimate sensor detectivity and noise equivalent power [1]. The fundamental performance limit of a thermal-based radiation sensor is notably reached when thermal coupling between the sensor and the surroundings is dominated by radiation (i.e., $x_{rad} \approx 1$) [4, 6, 17].

Efforts have been devoted to investigating the thermal properties [42, 43, 53] of SiN membranes such as thermal conductivity, heat capacity, diffusivity and thermal expansion coefficient. Emissivity of metal coating on SiN membranes have also been investigated in the context of electron microscopy [54]. Meanwhile, others have provided finite element simulation [55] of temperature profiles SiN membranes. Nevertheless, to the best of our knowledge, there is still no closed-form analytical expression describing fundamental thermal coupling quantities in such membranes.

Our goal is to provide expression for τ; for the heat conduction between the membrane

and the environment (G, in W/K); and for the fraction (x_{rad}) of this conduction that occurs via thermal radiation. We provide these expressions for the specific case of SiN films of square and circular shape in vacuum (i.e., in the absence of convection heat transfer), considering small temperature differences between the film and its environment.

4.2.3 Heat transfer in free-standing thin-films

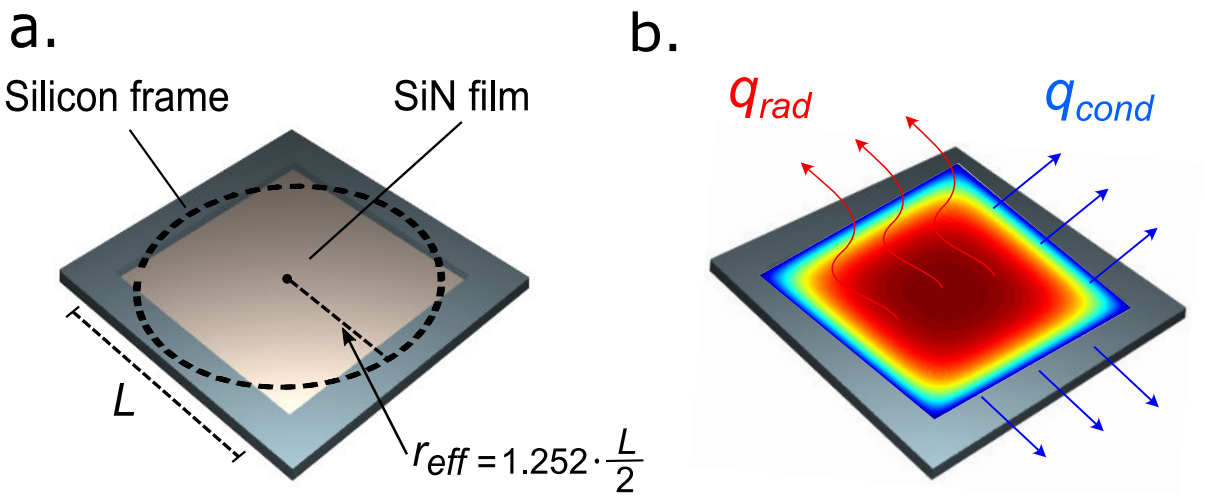

Figure 4.2: *(a) Square-shape SiN membrane and silicon frame. (b) Surface temperature profile of the SiN film with uniform internal generation.* q_{rad} *and* q_{cond} *denote the heat flux transferred via radiation and conduction, respectively.*

In order to calculate thermal coupling between a freestanding film and its environment, we consider volumetric heat generation ($\dot{q}$, in W/m^3) occurring uniformly within the membrane. From a heat transfer standpoint, such internal generation is mathematically analogous to uniform absorption of radiation from an external radiation source (e.g., in the context of radiation sensors). As a result of this internal generation, membrane temperature (T_m) rises relative to ambient (T_∞), and heat leaves the membrane by conduction to the silicon frame (q_{cond}, in W), and re-emission of radiation to the environment (q_{rad}, in W), as shown in Fig. 4.2(b). For example, an extreme case in which the membrane would be perfectly coupled to its environment via radiation would yield $q_{cond} = 0$, and $q_{rad} = q$, where $q = \dot{q}V$ and V is the membrane volume. We neglect

the contribution of convective heat transfer, an assumption representative of a system in vacuum as in most optomechanics and thermal radiation sensing experiments. In steady state, heat flux out of the heated membrane must equal heat generation inside the membrane, yielding the general heat equation:

$$-k \cdot \nabla^2 T_m + \dot{q}_{rad} = \dot{q}, \tag{4.7}$$

where k is the membrane conductivity, and T_m is the position-dependent membrane temperature. In Eq. (4.7), $\dot{q}_{rad}$ is the radiative exchange, per unit volume, between membrane and the environment at T_∞; is it given by:

$$\dot{q}_{rad} = \frac{2\sigma\epsilon(T_m^4 - T_\infty^4)}{d}, \tag{4.8}$$

where d is the membrane thickness, σ is Stefan-Boltzmann constant, and ϵ is the total hemispherical emissivity of SiN. The factor 2 accounts for emission on both faces of the membrane. We consider Dirichlet boundary conditions, setting the temperature of the SiN membrane edges as equal to ambient temperature (T_∞). In order words, we consider the silicon frames as strongly connected to the ambient environment via solid-state conduction, owing the high thermal conductivity of silicon.

The non-linear nature of radiative heat exchange ($\dot{q}_{rad} \propto T_m^4$) prevents direct derivation of a closed-form solution of the heat equation. We consequently linearize Eq. (4.8) by considering a small temperature difference between the membrane and the environment, yielding:

$$\dot{q}_{rad} \approx \frac{8\sigma\epsilon T_\infty^3}{d}(T_m - T_\infty). \tag{4.9}$$

This linearization results in $\approx 5\%$ error in when $(T_m - T_\infty) = 10\,\mathrm{K}$, and $< 1\%$ error when the temperature difference is 1 K. Such margin of error is reasonable for the general case of membranes in equilibrium with their environment, and for the specific case of uncooled radiation sensors aiming to resolve small temperature variations (with typical $T_m - T_\infty$

in the millikelvin range).

Due to the minute scale thickness of the SiN film (i.e., on the order of a few hundred nanometers), we consider uniform temperature along the direction normal to the surface, thus reducing Eq. (4.7) to a two-dimensional problem.

For a circular membrane of radius r_0, the solution to the linearized heat equation in cylindrical coordinates is conveniently simple:

$$T_m(r) = [1 - \frac{I_0(\beta \cdot r)}{I_0(\beta \cdot r_0)}] \cdot \frac{\dot{q}}{k \cdot \beta^2} + T_\infty, \tag{4.10}$$

where

$$\beta = \sqrt{\frac{8\sigma\epsilon T_\infty^3}{kd}}, \tag{4.11}$$

and I_N is the N^{th} order modified Bessel function of the first kind. Moreover, by integrating $T_m(r)$ over the area of the membrane, the average temperature $\overline{T_m}$ is expressed by:

$$\overline{T_m} = [1 - \frac{2}{\beta \cdot r_0} \cdot \frac{I_1(\beta \cdot r_0)}{I_0(\beta \cdot r_0)}] \cdot \frac{\dot{q}}{k\beta^2} + T_\infty. \tag{4.12}$$

From the position-dependent temperature profile in Eq. (4.10), we calculate heat transfer by conduction at the boundaries, using Fourier law of conduction:

$$q_{cond} = -2k\pi r_0 d \cdot \frac{\partial T_m}{\partial r}\Big|_{r_0}, \tag{4.13}$$

which yields:

$$q_{cond} = \frac{2q}{\beta \cdot r_0} \cdot \frac{I_1(\beta \cdot r_0)}{I_0(\beta \cdot r_0)}. \tag{4.14}$$

From Eq. (4.14), we can finally calculate the fraction of heat that leaves the membrane by radiation (x_{rad}):

$$x_{rad} = \frac{q_{rad}}{q} = 1 - \frac{q_{cond}}{q} = 1 - \frac{2}{\beta \cdot r_0} \cdot \frac{I_1(\beta \cdot r_0)}{I_0(\beta \cdot r_0)}. \tag{4.15}$$

In Eq. (4.15), we note that the right-hand side depends only on intrinsic membrane properties (i.e., independent of $\dot{q}$). As such, solving for $x_{rad} > 0.5$ yields the properties required for a membrane to be thermally coupled to its environment more strongly via radiation than via solid-state conduction.

From the temperature profile of the membrane [see Eq. (4.10)], we can also express the thermal time constant of the membrane (τ, in s) and its overall thermal conductance with the environment (G, in W/K), both of which are of particular importance for use in sensors [1], and for predicting noise profiles in micro resonators [50, 51, 52]. Note that $G = G_{cond} + G_{rad}$ includes heat transfer both by conduction in the supporting frame (G_{cond}) and by radiation (G_{rad}). We obtain G and τ by evaluating the average temperature ($\overline{T}_m$) of the membrane [i.e., by integrating Eq. (4.10)] and using:

$$G = \frac{q}{\overline{T}_m - T_\infty} = \frac{k\pi(\beta \cdot r_0)^2 d}{1 - \frac{2}{\beta \cdot r_0} \cdot \frac{I_1(\beta \cdot r_0)}{I_0(\beta \cdot r_0)}}, \tag{4.16}$$

$$\tau = \frac{c_p \rho V}{G} = \frac{c_p \rho [1 - \frac{2}{\beta \cdot r_0} \cdot \frac{I_1(\beta \cdot r_0)}{I_0(\beta \cdot r_0)}]}{k\beta^2}, \tag{4.17}$$

where c_p and ρ are respectively the specific heat capacity and the material density. We note that, when heat transfer becomes entirely dominated by radiation (i.e. for large areas), Bessel terms become negligible and both expressions simplify to radius-independent quantities:

$$G_{rad} = 8A\sigma\epsilon T_\infty^3, \tag{4.18}$$

$$\tau_{rad} = \frac{\rho c_p d}{8\sigma\epsilon T_\infty^3}. \tag{4.19}$$

For a square membrane—a geometry much more frequently encountered in practice—

an analytical solution to the linearized heat equation also exists, but comprises an infinite amount of Fourier terms in order to respect the boundary conditions ($T = T_\infty$ at the membrane edges). Rather than using this complex solution, we numerically solve for the temperature profile of a square membrane using finite element analysis. From this solution (see Appendix Fig. A1), we determine that the radiative thermal coupling ratio ($x_{rad} = q_{rad}/q$) of a square membrane of side length L matches that of a circular membrane if we consider an effective radius:

$$r_{eff} = 1.252\frac{L}{2}. \tag{4.20}$$

Logically, this effective radius falls between half of a square membrane side length ($L/2$), and half of its diagonal ($L/\sqrt{2}$), as shown schematically in Fig. 4.2(a). By replacing Eq. (4.20) in Eq. (4.15), the fraction of heat transfer occurring by radiation in a square membrane (x_{rad}) is given by:

$$x_{rad} = 1 - \frac{2}{\beta \cdot r_{eff}} \cdot \frac{I_1(\beta \cdot r_{eff})}{I_0(\beta \cdot r_{eff})}. \tag{4.21}$$

The total thermal conductance of a square membrane is subsequently:

$$G = \frac{G_{rad}}{x_{rad}} = \frac{8L^2\sigma\epsilon T_\infty^3}{x_{rad}}, \tag{4.22}$$

while τ is now given by:

$$\tau = \frac{c_p\rho d}{8\sigma\epsilon T_\infty^3}x_{rad}. \tag{4.23}$$

Eq. (4.23) yields an aberrant $\tau \approx 0$ when $x_{rad} \approx 0$, but this result occurs for $L \approx 0$, in which case our assumption of a 2-D problem (i.e., $L >> d$) does not hold.

4.2.4 Emissivity of SiN films

From Eq. (4.15) to Eq. (4.23), it is obvious that the total hemispherical emissivity (ϵ) is a key parameter governing radiative heat transfer in free-standing membranes. We calculate ϵ for the specific case of SiN using Kirchhoff law—i.e., directional spectral emissivity is equal to absorption:

$$\epsilon_{\lambda,\theta}(\lambda,\theta) = \alpha_{\lambda,\theta}(\lambda,\theta). \tag{4.24}$$

We calculate $\alpha_{\lambda,\theta}(\lambda,\theta) = 1 - R_{\lambda,\theta}(\lambda,\theta) - T_{\lambda,\theta}(\lambda,\theta)$ using conventional optical multi-layer calculation [56] with the complex permittivity of SiN taken from [57]. For film thicknesses of several nanometers, the permittivity of dielectrics is commonly assumed as independent from thickness [58], hence we consider constant permittivity in our calculations. R and T denote the optical power reflection and transmission coefficients, respectively. We find that these coefficients depend non-negligibly on the angle, such that we integrate the emissivity according to Lambert's cosine law to obtain [39]:

$$\epsilon_{\lambda}(\lambda) = 2\int_0^{\pi/2} \epsilon_{\lambda,\theta}(\lambda,\theta)\cdot cos(\theta)\cdot sin(\theta)d\theta, \tag{4.25}$$

which is plotted in Fig. 4.3(a) for the specific example of a 100 nm thick membrane. In comparison, the normal directional spectral emissivity $\epsilon_{\lambda,\theta}(\lambda,0)$ is roughly 25% higher than the integrated value $\epsilon_{\lambda}(\lambda)$. In other words, emission and absorption are slightly stronger at normal incidence. This may be beneficial for radiation sensing applications [1] where a sensor should be more strongly coupled at normal incidence (i.e. pointing at the object to be detected). We finally obtain the total hemispherical emissivity ϵ by weighting $\epsilon_{\lambda}(\lambda)$ with the blackbody emission spectrum $E_{\lambda,b}(\lambda,T)$ at temperature T:

$$\epsilon(T) = \frac{\int_0^{\infty} \epsilon_{\lambda}(\lambda)\cdot E_{\lambda,b}(\lambda,T)d\lambda}{E_b(T)}, \tag{4.26}$$

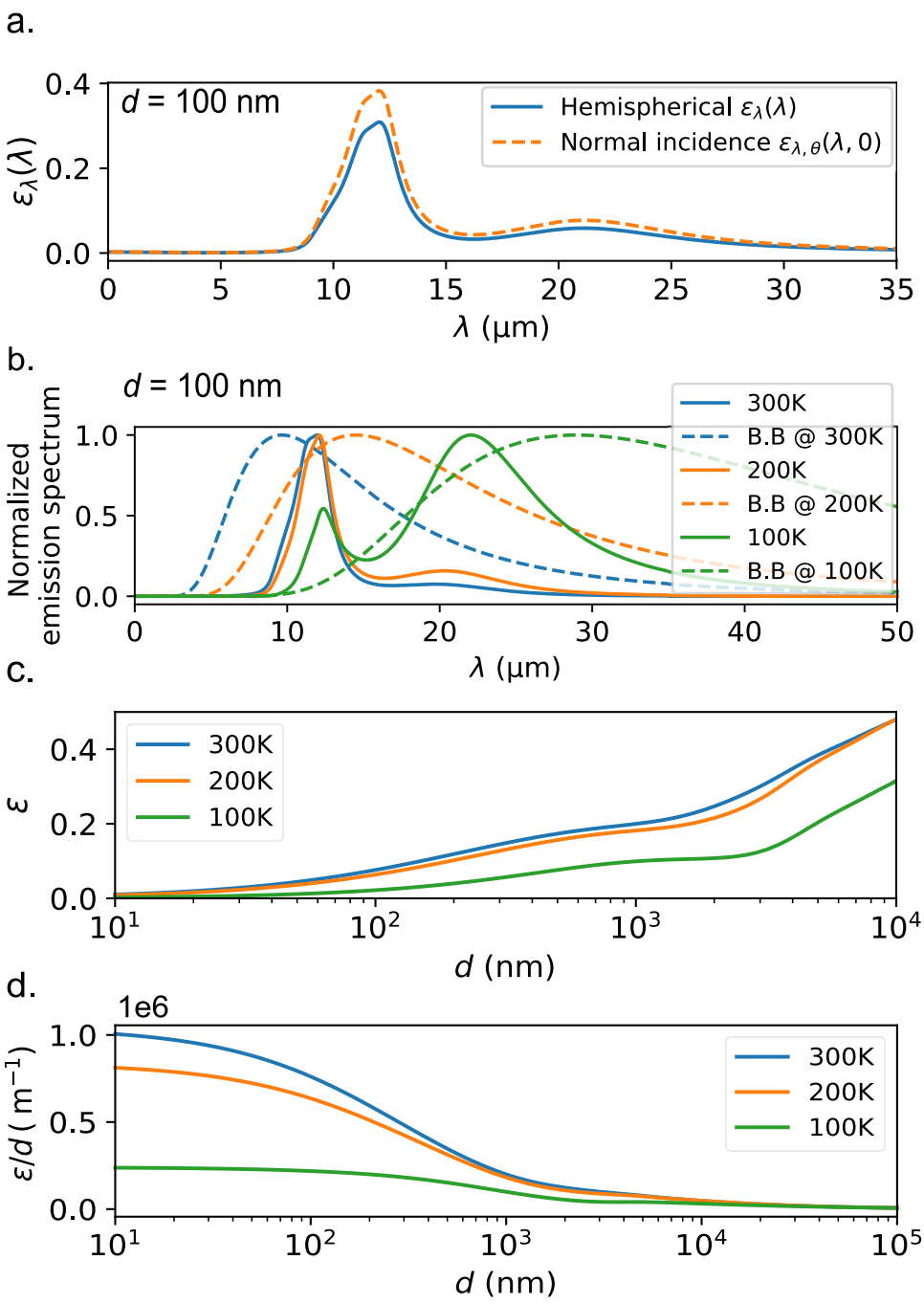

Figure 4.3: *(a) Comparison between normal and hemispherical emissivity for free-standing SiN membranes. (b) Normalized emission spectrum of a 100 nm thick SiN membrane at different temperatures. Dashed lines represent blackbody spectra. As temperature decreases, the peak of the emission spectrum moves towards longer wavelengths. (c) Hemispherical total emissivity of free-standing SiN membranes at different temperatures. (d) Hemispherical total emissivity normalized by film thicknesses for different temperatures. This quantity scales with of the fraction of heat transfer occurring by radiation (x_{rad}) and is maximized for lower membrane thicknesses.*

where $E_b(T) = \sigma T^4$. For concision, we use the notation $\epsilon(T) = \epsilon$ in this work. This weighting is shown, for various membrane temperatures, in Fig. 4.3(b) while ϵ as a function of thicknesses, is presented in Fig. 4.3(c). We find that both the emission distribution Fig. 4.3(b) and ϵ Fig. 4.3(c) weakly depend on temperature unless cryogenic membrane temperatures (e.g., 100 K) are considered.We willingly omit calculations at very low temperatures ($< 1\,\mathrm{K}$) as this would presumably require a different model for material properties of SiN. We also note that the hemispherical emissivity for thin films is a strong function of thickness. This emphasizes that the common assumption of $\epsilon \approx 0.6$ [4] for SiN appears appropriate only for bulk SiN materials and not for thin films.

We note that thicker films lead to higher emissivity [see Fig. 4.3(c)]—however as shown in Eq. (4.11), the relevant quantity for estimating the contribution of radiation to the total heat transfer is the ratio ϵ/d. This is plotted in Fig. 4.3(d), from which we conclude that, for a given surface area, thinner membranes are more efficiently coupled via radiation. The thickness dependence is the strongest in the 100 nm – 1 μm range, while the relation reaches a relative plateau for thickness commonly employed in opto-mechanics experiments ($d < 100\,\mathrm{nm}$) [8].

Having calculated the ϵ/d ratio, we can determine the critical membrane length for which heat transfer is dominated by radiation (i.e., $x_{rad} > 0.5$). Using the closed-form relation developed in Eq. (4.21), we plot x_{rad} as a function of $\beta \cdot r_{eff}$ in Fig. 4.4(a). The β value for SiN, for given d and T_m, is given in Fig. 4.4(b). We note that Fig. 4.4(a) is a universal relation for any freestanding thin film membrane anchored on all sides, while Fig. 4.4(b) accounts for the specific case of SiN. In Fig. 4.4(a), we find that thermal coupling of free-standing thin films is radiation dominated for $\beta \cdot r_{eff} \approx 3.33$. From this, we finally derive a simple expression for the threshold of a radiation-coupled membrane:

$$r_{eff} > \frac{3.33}{\beta} = 3.33\sqrt{\frac{kd}{8\sigma\epsilon T_\infty^3}}, \tag{4.27}$$

for which the ϵ/d ratio can be obtained graphically from Fig. 4.3(d), in the specific case

of SiN. We note that this equation is the same for a circular membrane, using $r_{eff} = r_0$ in lieu of $r_{eff} = 1.252L/2$ for a square membrane.

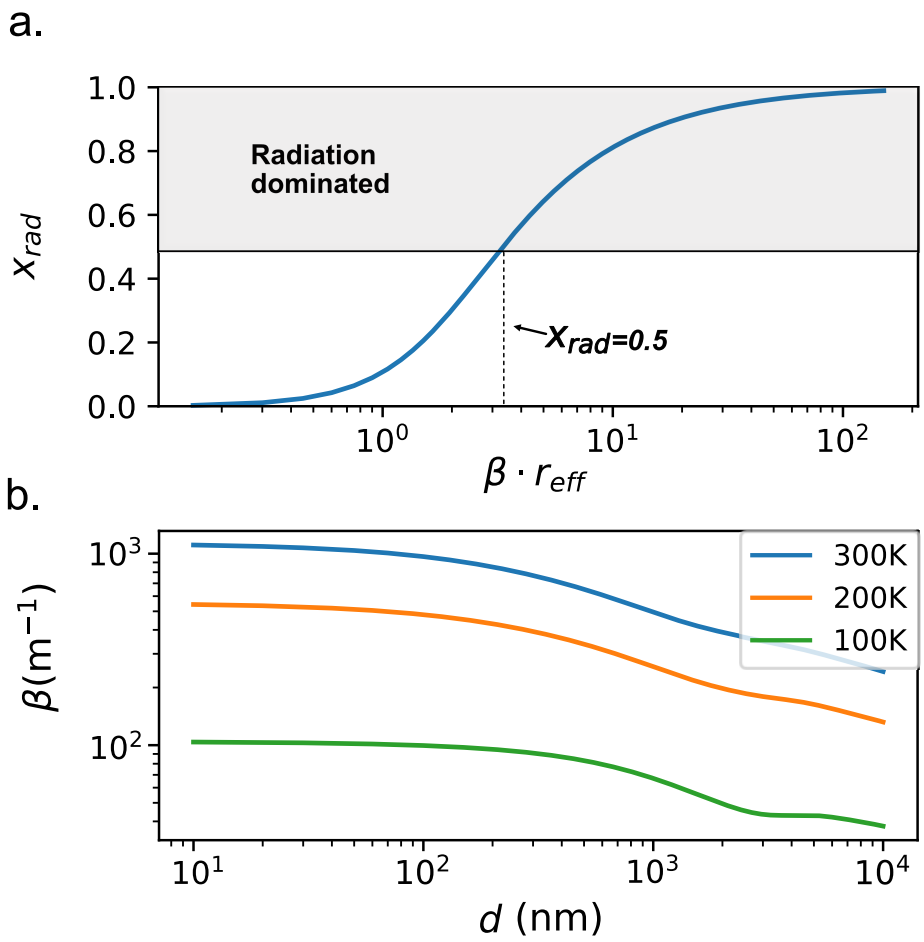

Figure 4.4: *(a) Fraction of total heat transfer occurring via radiation (x_{rad}) in free-standing membranes as a function of $\beta \cdot r_{eff}$. The model applies both to circular ($r_{eff} = r_0$) and square ($r_{eff} = 1.252L/2$) membranes. For x_{rad} larger than 0.5, membrane thermal coupling is radiation-dominated. (b) β as a function of membrane thickness for the specific case of SiN*

4.2.5 Temperature induced frequency shifts

A central consequence of temperature changes in thin-film membranes is resonance frequency shift [17, 15, 6], due to varying in-plane stress σ. For the simple case of circular membrane with uniform internal generation, the membrane stress does not depend on azimuthal coordinates and can be expressed by the sum of a constant, temperature-independent term (e.g., $\sigma_0 \approx 100$ Mpa) and a radius-dependent term (σ_r):

$$\sigma = \sigma_0 + \sigma_r, \tag{4.28}$$

σ_r can be expressed as [15, 59]:

$$\sigma_r = -\alpha E(\frac{1}{r^2}\int_0^r r\Delta T_m(r)dr + \frac{1+\nu}{1-\nu}\frac{\Delta\overline{T_m}}{2}). \tag{4.29}$$

where $\Delta\overline{T_m} = \overline{T_m} - T_\infty$, α is the thermal expansion coefficient of the membrane material, E is the Young's modulus and ν is the Poisson ratio. If we approximate the membrane temperature as uniform (i.e., $T_m(r) = \overline{T_m}$), σ_r simplifies to a radius-independent term:

$$\sigma_r = -\frac{\alpha E}{1-\nu} \cdot \Delta\overline{T_m}. \tag{4.30}$$

Hence, the membrane frequency shift (Δf) can be linked to the membrane average temperature change ($\Delta\overline{T_m}$) using Eq. (4.31), for small temperature variations [6]:

$$\Delta f \approx -\frac{\alpha E f_0}{2\sigma_0(1-\nu)}\Delta\overline{T_m}, \tag{4.31}$$

We find that by approximating a constant membrane temperature in Eq. (4.30-4.31) results in reasonable error compared to considering rigorous radius dependant stress [Eq. (4.29)]. In Fig 4.5, we perform finite element simulation (See Appendix A2) considering a non-uniform temperature profile and we compare those to the uniform temperature

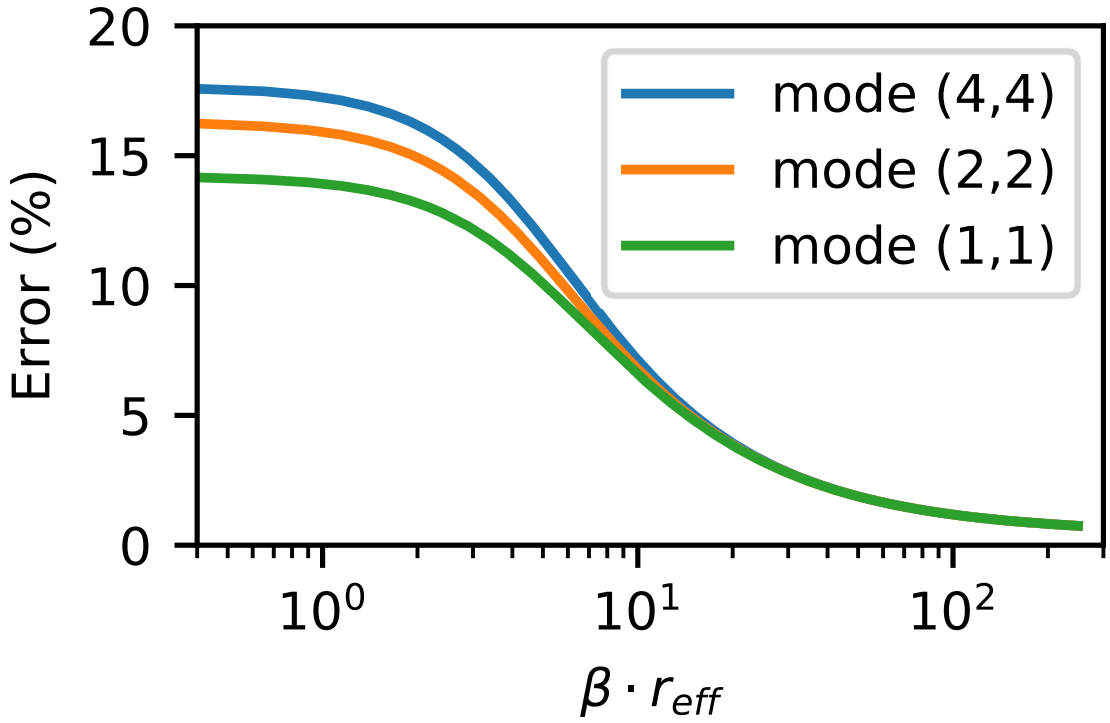

Figure 4.5: *Error percentage in estimating resonance frequency shift (Δf) using a position-independent, average membrane temperature simulation performed at $\Delta\overline{T_m} = 10k$.*

approximation. We find that the uniform temperature profile assumption is particularly accurate in the case of large membrane sizes (i.e., radiation dominated). In the worst-case scenario, the uniform temperature approximation underestimates the frequency shift by 20% for conduction-dominated, high order modes (See Fig. 4.5).

4.2.6 Experimental results

We conduct preliminary experiments for one membrane geometry and find that our model is in agreement with experimental results. We use a commercially available (3×3 mm side length, 200 nm thickness) low stress SiN membrane, where a membrane Young's modulus $E = 300\,\mathrm{GPa}$, a thermal expansion coefficient $\alpha = 2.2 \times 10^{-6}\,\mathrm{K}^{-1}$ [60] and a tensile stress $\sigma_0 \approx 100\,\mathrm{Mpa}$. We infer the membrane temperature from its resonance frequency using Eq. (4.31) and considering a ≈18% correction in $\Delta\overline{T_m}$ taken from Fig. 4.5 (See Appendix A2 for details about the correction). We also consider a 25% uncertainty for this relation given the variability of material constants and on the membrane dimensions [see error bars in Fig. 4.6(c)]. The experiment is conducted in high vacuum ($1.5 \times 10^{-6}\,\mathrm{torr}$) to eliminate convection heat transfer and viscous damping by air.

We vary the temperature of the SiN membrane by exposing it to a rough-surfaced aluminum oxide heater [see Fig. 4.6(b)] placed within a short distance (5 mm) from the membrane. We infer the heater temperature by correlating it to its electrical resistance using a temperature coefficient of resistance of $4.7 \times 10^{-3}\,\mathrm{K}^{-1}$. We measure this value in a separate experiment by placing the heater on a hot plate and by measuring its resistance as a function of temperature. Due to the variability in documented value for the total hemispherical emissivity of rough-surfaced aluminum oxide [39], we assume an upper bound value of $\epsilon_{heater} = 0.8$ and a lower bound of 0.6. A reflective aluminum shield is placed between the membrane and the heater to prevent the silicon frame of the membrane from heating up upon absorption of radiation. A piezoelectric actuator is attached to the same glass slide as the membrane to excite its mechanical resonance. Membrane displacement is measured using an optical interferometer setup [34]. The instantaneous resonance (f) of the SiN membrane shifts by over 1 KHz when subject to a 70 K increment in heater temperature, as presented in Fig. 4.6(c).

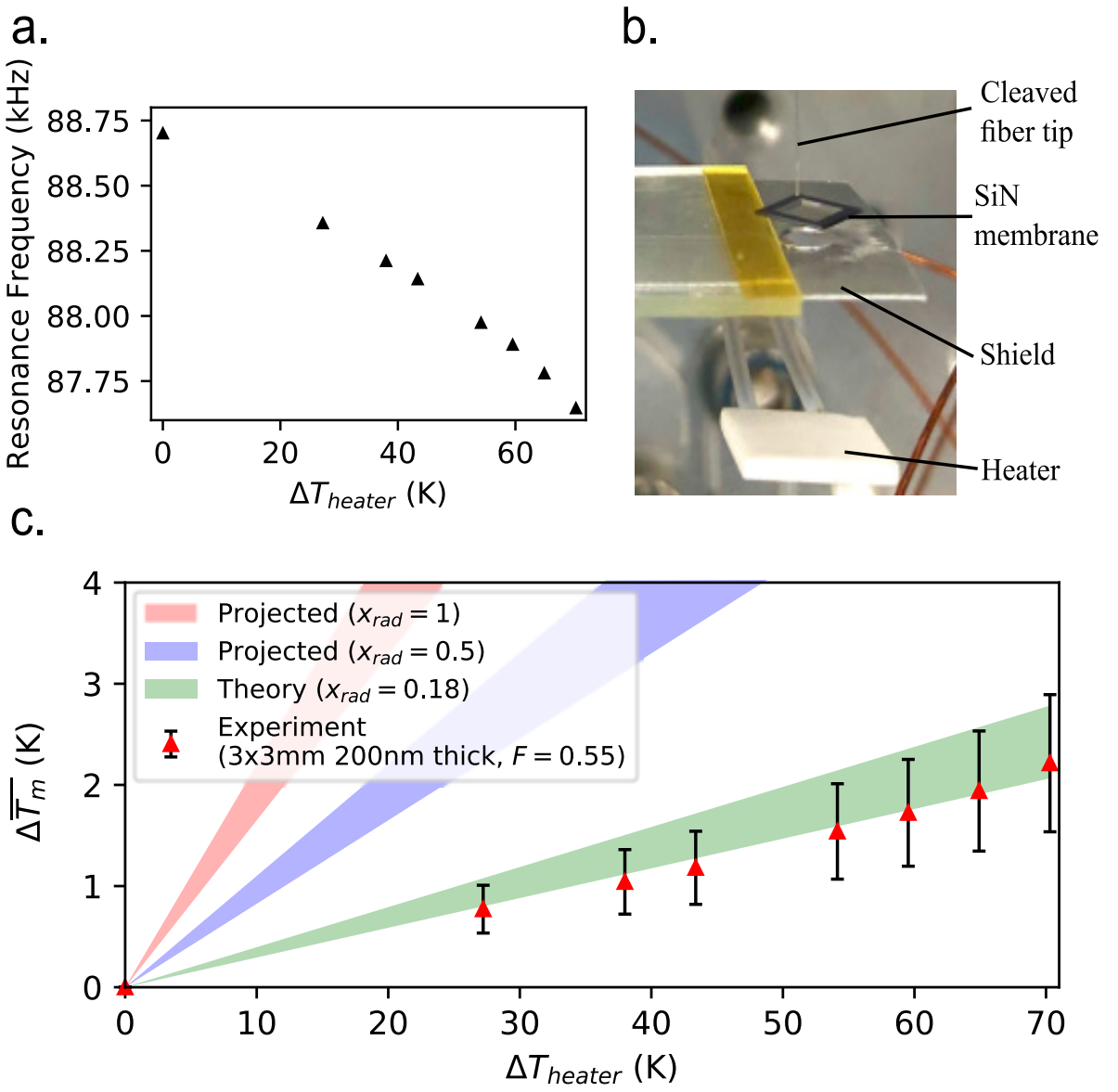

Figure 4.6: *(a) Resonance frequency of mechanical mode 2, 2 as a function of heater temperature. (b) Photograph of the experimental setup inside the vacuum chamber. For the actual experiment, the heater is placed closer (5 mm) from the membrane but is displaced here for a clearer picture. (c) Membrane temperature as a function of heater temperature. Experimental results agree with our model within a 25% error on the membrane material constants. Predicted theoretical results for $x_{rad} = 0.5$ and 1 are also shown for illustrative purpose, for the same $F = 0.55$ view factor. Shaded areas are bounded by the range $\epsilon_{heater} = 0.6$ and 0.8.*

By neglecting photons having more than one interaction with the heater and membrane (due to the relatively small size of the membrane, the diffusive surface of the heater,

and its high emissivity/absorptivity) the temperature of the membrane is correlated to the heater temperature simply by:

$$\Delta T_m \approx \frac{\Delta T_{heater}}{2} \cdot x_{rad} \cdot F \cdot \epsilon_{heater} \tag{4.32}$$

where, $F = 0.55$ is the geometrical view factor [39]. The detailed thermal equivalent circuit from which Eq. (4.32) derived is given in Appendix Fig. (A3). From Eq. (4.32), correlating the membrane temperature with the heater temperature allows measurement of x_{rad} and shows good agreement with our model. This is presented in Fig. 4.6(c), where the experimental points fall within the theoretical values from Eq. (4.21). For illustrative purpose, we also plot the projected values for a membrane that would be on the threshold ($x_{rad} = 0.5$) or completely radiation-dominated ($x_{rad} = 1$), for the same geometrical view factor ($F = 0.55$).

4.2.7 Conclusion

We expect that our work will be of interest for achieving high performance radiation sensors exploiting the high temperature sensitivity of SiN mechanical resonance [17]. In such sensors, one would ideally want to achieve $x_{rad} \approx 1$ to reach the highest possible detectivity [1]. Our work shows that achieving such x_{rad} value is feasible using realistic membrane dimensions. We readily achieve $x_{rad} = 0.18$ using commercially available SiN membranes of non-optimized dimensions. We also expect that the provided closed-form expressions for τ and G will be of great use for predicting frequency noise in high Q-factor SiN [50, 51, 52]. Given the high temperature sensitivity of resonance frequency in SiN resonators, we expect temperature fluctuation noise—which is directly linked to τ and G [52] —to have a non-negligible contribution to frequency noise. Finally, we expect that outlining the non-negligible contribution of radiative heat transfer may be useful in experiments involving cooling of SiN membranes. As a striking example, a membrane

with $x_{rad} > 0.5$ could be more efficiently cooled by a cold object facing it, than by direct contact cooling of its supporting silicon frame.

4.3 Heat transfer model in 1-D

In the pre-print paper, we presented the full detailed derivation of the heat transfer model in 2-D [see Eq. (4.7) to Eq. (4.23)], however, it is also worth to solve this heat transfer problem in 1-D as a reference and fully exhibits the characteristics of this model. Hence, in this section, we follow the similar procedure as in Section. (4.2.3) to present the derivation of the heat transfer model in 1-D.

In 1-D model, we also consider the external radiation as the volumetric heat source $q = \dot{q}V$ and neglect the contribution of convective heat transfer, an assumption representative of a system in vacuum as in most optomechanics and thermal radiation sensing experiments. In steady state, heat flux out of the heated membrane must equal heat generation inside the membrane, yielding the general heat equation:

$$-k \cdot \nabla^2 T_m + \dot{q}_{rad} = \dot{q}, \tag{4.33}$$

where k is the membrane conductivity, and T_m is the position-dependent membrane temperature. In Eq. (4.33), $\dot{q}_{rad}$ is the radiative exchange, per unit volume, between membrane and the environment at T_∞; is it given by:

$$\dot{q}_{rad} = \frac{2\sigma\epsilon(T_m^4 - T_\infty^4)}{d}, \tag{4.34}$$

where d is the membrane thickness, σ is Stefan-Boltzmann constant, and ϵ is the total hemispherical emissivity of SiN. The factor 2 accounts for emission on both faces of the membrane. We consider Dirichlet boundary conditions, setting the temperature of the SiN membrane edges as equal to ambient temperature (T_∞). In order words, we

consider the silicon frames as strongly connected to the ambient environment via solid-state conduction, owing the high thermal conductivity of silicon.

The non-linear nature of radiative heat exchange ($\dot{q}_{rad} \propto T_m^4$) prevents direct derivation of a closed-form solution of the heat equation. We consequently linearize Eq. (4.34) by considering a small temperature difference between the membrane and the environment, yielding:

$$\dot{q}_{rad} \approx \frac{8\sigma\epsilon T_\infty^3}{d}(T_m - T_\infty). \tag{4.35}$$

This linearization results in $\approx 5\%$ error in when $(T_m - T_\infty) = 10\,\mathrm{K}$, and $< 1\%$ error when the temperature difference is 1 K. Such margin of error is reasonable for the general case of membranes in equilibrium with their environment, and for the specific case of uncooled radiation sensors aiming to resolve small temperature variations (with typical $T_m - T_\infty$ in the millikelvin range).

Here, since we are solving heat transfer model in 1-D, Eq. (4.35) becomes an ordinary differential equation which the temperature profile only changes with respect to the x-axis. For a square membrane of side length L, the solution to the linearized 1-D heat equation in Cartesian coordinates is conveniently simple:

$$T_m(x) = [1 - \frac{\cosh(\beta \cdot x)}{\cosh(\beta \cdot L/2)}] \cdot \frac{\dot{q}}{k \cdot \beta^2} + T_\infty, \tag{4.36}$$

where

$$\beta = \sqrt{\frac{8\sigma\epsilon T_\infty^3}{kd}}, \tag{4.37}$$

From this temperature profile, we calculate heat transfer by conduction at the boundaries, using Fourier law of conduction:

$$q_{cond} = -2kLd \cdot \frac{\partial T_m}{\partial x}\Big|_{L/2}, \tag{4.38}$$

which yields:

$$q_{cond} = \frac{2q}{\beta \cdot L} \cdot \tanh(\beta L/2). \tag{4.39}$$

From Eq. (4.39), we can finally calculate the fraction of heat that leaves the membrane radiation (x_{rad}):

$$x_{rad} = \frac{q_{rad}}{q} = 1 - \frac{q_{cond}}{q} = 1 - \frac{2}{\beta \cdot L} \tanh(\beta L/2). \tag{4.40}$$

In Eq. (4.40), we note that the right-hand side depends only on intrinsic membrane properties (i.e., independent of $\dot{q}$). As such, solving for $x_{rad} > 0.5$ yields the properties required for a membrane to be thermally coupled to its environment more strongly via radiation than via solid-state conduction.

From the 1-D temperature profile of the membrane [see Eq. (4.36)], we can also express the thermal time constant of the membrane (τ, in s) and its overall thermal conductance with the environment (G, inW/K), both of which are of particular importance for use in sensors [1], and for predicting noise profiles in micro resonators [50, 51, 52]. Note that $G = G_{cond} + G_{rad}$ includes heat transfer both by conduction in the supporting frame (G_{cond}) and by radiation (G_{rad}). We obtain G and τ by evaluating the average temperature ($\overline{T}_m$) of the membrane [i.e., by integrating Eq. (4.36)] and using:

$$G = \frac{q}{\overline{T}_m - T_\infty} = \frac{k(\beta \cdot L)^2 d}{1 - \frac{2}{\beta \cdot L} \cdot \tanh(\beta L/2)}, \tag{4.41}$$

$$\tau = \frac{c_p \rho V}{G} = \frac{c_p \rho [1 - \frac{2}{\beta \cdot L} \cdot \tanh(\beta L/2)]}{k\beta^2}, \tag{4.42}$$

where c_p and ρ are respectively the specific heat capacity and the material density.

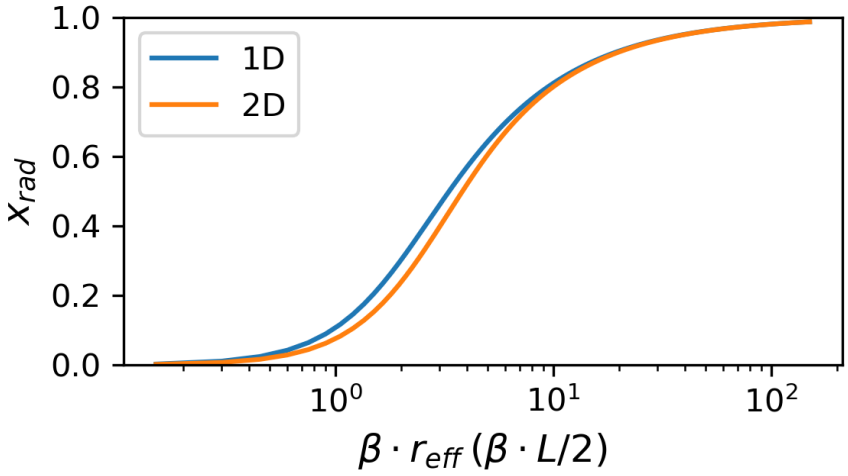

Figure 4.7: *x_{rad} comparison between 1D and 2D analysis.*

Using derived Eq. (4.40), we can compare the x_{rad} in 1D to 2D. The results from Fig. (4.7) validates the rigidity of our heat transfer model, which the overall shape of these two curves highly match with each other. However, we can also see that the 2D curve sits slightly below the 1D curve. This effect shows that it requires larger membrane dimension to achieve radiation-dominated heat transfer when consider 2D heat flow.

5. Thesis Conclusion & Future Work

5.1 Conclusion

In this work, we experimentally demonstrate the fundamental working principle of a opto-mechanical radiation sensor using a SiN membrane resonators. More importantly, we derive a closed-form universal heat transfer model for conveniently estimating the thermal coupling of any square or circular shaped thin-film membrane and other system parameters such as the thermal conductivity and the thermal time constant. The developed model is in good agreement with the experimental results. We also have performed a multi-layer calculation for computing the emissivity of the low stress thin-film silicon nitride membrane. This calculation is presented as a graphical result which can be used to estimate the emissivity of a SiN membrane at different thicknesses and temperatures. Our developed heat transfer model is not only useful to resonator-based radiation sensor, but also can be implemented to evaluate the thermal coupling conditions of virtually any other devices that involves thin-film membranes.

Many resonator-based bolometers have already utilized the resonant sensing scheme to avoid the performance trade-off which caused by electrical sensing scheme. However, they are still two orders of magnitude below the fundamental detectivity limit of thermal detector ($D^* = 1.8 \times 10^{10}$ cmHz$^{1/2}$W^{-1}) which is in part due to their inefficient thermal coupling with the environment (i.e., $x_{rad} < 0.5$). For the commercial SiN membrane sample (3×3 mm, 200 nm) that is used in our preliminary experiment, we reach a x_{rad} value of ≈ 0.18 which is also below the critical value of 0.5. The radiation dominated membrane size (i.e., $x_{rad} \approx 1$) is under the process of fabrication and its performance needs to be tested to prove the fundamental detectivity limit can be reached by using this specific setup.

5.2 Future works

- Although we have demonstrated the effectiveness of the heat transfer model through our preliminary experiment using the commercially available SiN membranes, more experimental validation with different membrane sizes is still required. Hence, our colleague is in the progress of fabricating more squared-sized membrane with different side lengths. More importantly, the radiation-dominated sized membrane's performance needs to be tested, such as its detectivity, noise equivalent temperature difference, frequency stability, etc.

- An important aspect of our closed-form heat transfer model is to provide the thermal time constant of the SiN membrane. However, the thermal time constant could not be measured in existing experimental setup due to the slow thermal time constant of our ceramic heater. To measure the thermal time constant of the SiN membrane, we will have to use a radiation source that has faster thermal time constant than our membrane. This problem can be solved by using an amplitude modulated laser or a rotating optical chopper to mechanically modulate the radiation from the heater.

- In the current setup, we are using an external piezo-electric actuator to excite the membrane, which can be not scaled to real-world applications in the future. To create integrated mechanical drive, we can deposit metal electrodes on top of the SiN membrane. By using this metal deposition, we can also include a capacitive readout as a replacement for the optical readout which largely miniaturized the whole system.

- To track the resonance frequency more precisely, we can include a phase-lock loop in the system which automatically tracks the instantaneous resonance and feed the signal back to the drive to perform closed-loop actuation.

Appendix

A. Comparing numerical and analytical models

The 2-D steady-state temperature profile of the squre-sized SiN membrane is simulated using MATLAB PDE solver, such that the closed-form analytical results can be compared with the numerical simulation. We first define the computational geometry to be a square which has the same side length (3 mm) as the sample SiN membrane. We then specify the coefficients for the PDE model by rearranging the heat equation as:

$$-\nabla \cdot (\nabla T_m) + \beta^2 T_m = \frac{\dot{q}}{k} + \beta^2 T_\infty, \tag{A.1}$$

where σ is the Stefan-Boltzmann constant, ϵ is the total hemispherical emissivity of the 200 nm (d) SiN membrane which is calculate to be 0.11, T_∞ is the ambient temperature (293 K), k is the conductivity of the SiN membrane which is found to be 12 ($\mathrm{W/m \cdot K}$). Note that $\dot{q}$ is the heating power being absorbed by the SiN membrane per unit volume. Here we arbitrarily set $\dot{q}$ to the same value for both models (i.e., analytical and numerical). The simulated temperature profile is shown in Fig. A.1.

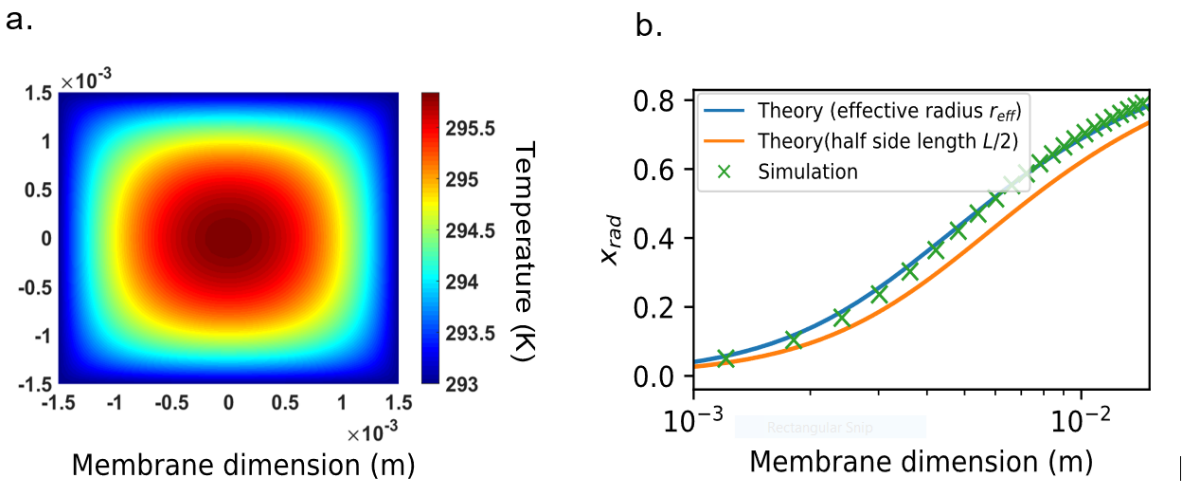

Figure A.1: *(a) 2-D temperature simulation for* 3×3 *mm, 200 nm SiN membrane. (b)* x_{rad} *as a function of side length which discrete points are given by the numerical simulation, whereas the continuous lines are plotted by closed-form expression.*

With the numerical simulation, we can obtain the fraction of heat that leaves the membrane by radiation (x_{rad}) using the simulated temperature profile. By plotting this result and the analytical results for many side lengths values, we find that the correction ratio between the effective radius and half of the side length to be 1.252 which is presented in Eq. (4.20).

B. Experimental temperature approximation of the SiN membrane

In our preliminary experiment, the average temperature increment $\Delta\overline{T_m}$ of the membrane is estimated by Eq. (4.31) with SiN membrane's material properties which assumes uniform temperature profile for computational simplicity. However, strictly speaking, the temperature of the membrane $T_m(r)$ is location dependent. This section of the supplementary is dedicated to investigating the error margin caused by the Eq. (4.31).

Besides from Eq. (4.31), we can also use the equation of motion to describe the vibration of a circular membrane:

$$\frac{1}{r}\frac{\partial}{\partial r}((\sigma_0+\sigma_r)r\frac{\partial U(r,t)}{\partial r})-\rho\frac{\partial^2 U(r,t)}{\partial t^2}=0 \tag{B.1}$$

and solve its eigenvalue to precisely calculate the resonance frequency f of the SiN membrane when considering a more realistic non-uniform temperature profile $T_m(r)$. Here, $U(r,t)$ represents the out-of-plane displacement of the membrane, σ_r is the position-dependent stress derived in the main text as Eq. (4.29). Due to the varying in-plane stress σ_r, the Eq. (B.1) can not be solved analytically. Thus, we use finite-element method to solve for its eigenvalues numerically through MATLAB PDE solver for different mechanical modes. By setting the same $\Delta\overline{T_m}$ to Eq. (B.1) and Eq. (4.29), we can see the discrepancy of these two methods in estimating resonance frequency shift Δf.

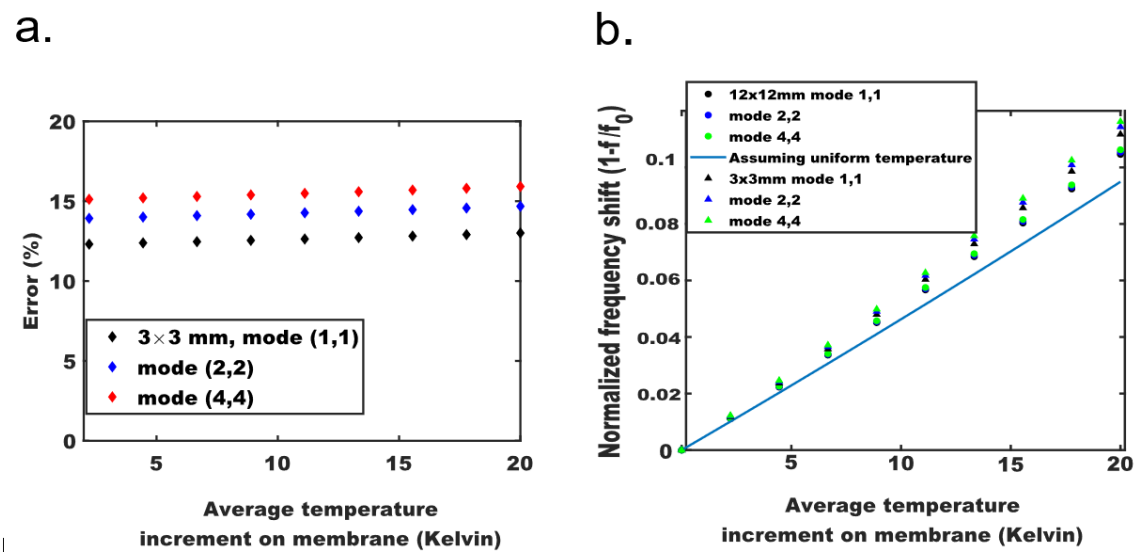

Figure B.1: *(a) Error of three non-degenerate modes caused by Eq. (4.29) as a function of average temperature increment for* 3×3 *mm membrane. (b) Normalized resonance shift calculated by two methods as a function of average temperature increment for different sizes and modes with the same 200 nm thickness.*

We compare the predicted frequency shift Δf by these two methods [Eq. (B.1) and Eq. (4.31)] when subjecting to the same and Fig. B.1(a) presents the percentage error for a 3×3 mm, 200 nm membrane which is used in our preliminary experiment. This result indicates that the error percentage is clearly affected by the order of mechanical mode (e.g., higher order mode induces larger error), but not by temperature increment on the membrane. In Fig. B.1(b), we note that the error of Δf for a larger sized membrane (i.e., radiation dominated sized membrane) is smaller.

By conducting this simulation for the specific case of 3×3 mm, 200 nm SiN membrane, we can use linear regression to fit the simulated data (see Fig. B.2) and calculate the discrepancy between these two models. We find that by using Eq. (4.31), the experimental average temperature increment of the membrane $\Delta\overline{T_m}$ is overestimated by 18.3%. This error is corrected accordingly in Fig. 4.6(c).

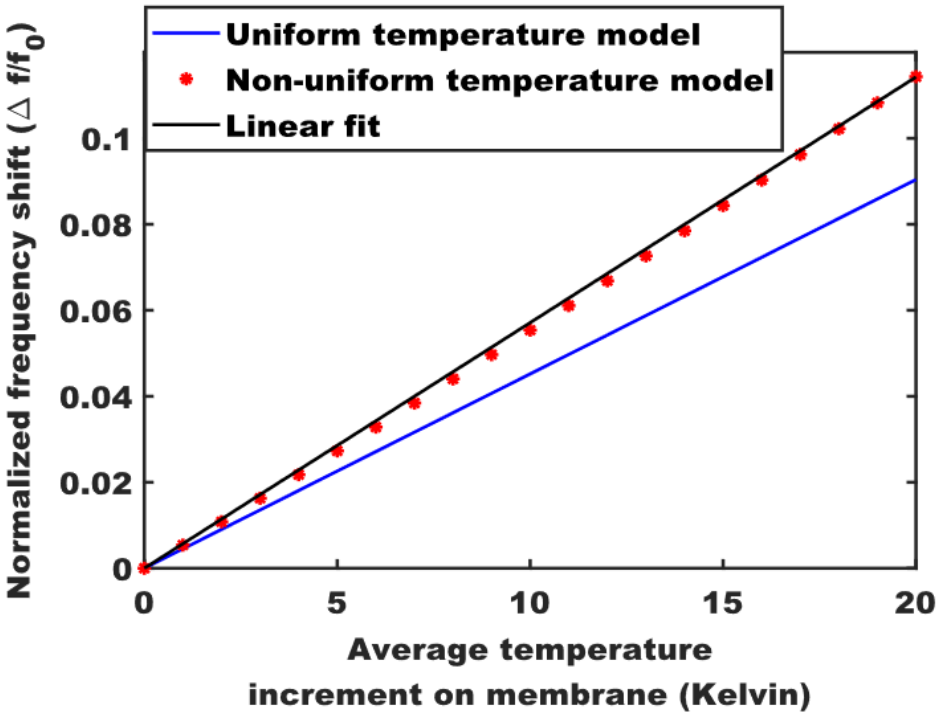

Figure B.2: *Normalized resonance shift calculated by two methods as a function of average temperature increment for* 3×3 *mm, 200 nm SiN membrane. The simulated data is fitted by linear regression.*

C. Thermal equivalent circuit

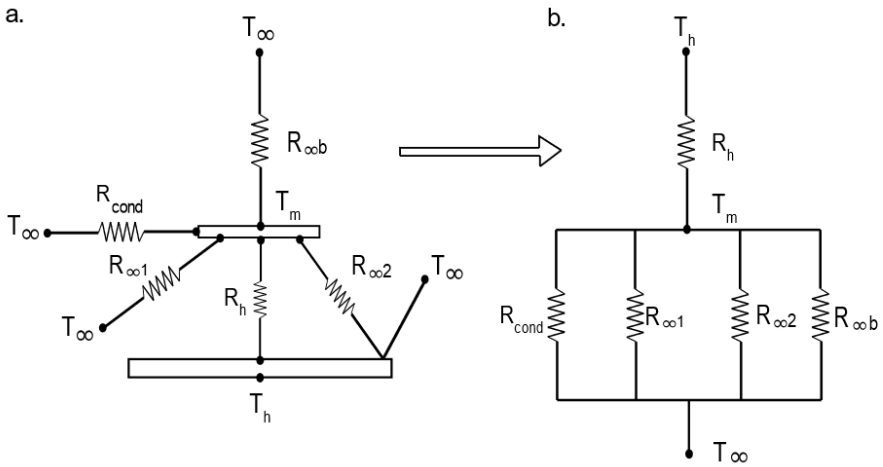

Figure C.1: *Thermal equivalent circuit considering the heater, the membrane, and the vacuum environment. (a) Thermal circuit schematic. (b) Simplified thermal circuit.*

The analogy of the electric circuit is useful to understand the heat transfer of the SiN membrane with its environment. Here we neglect multiple heat exchanges between the SiN membrane and the heater by only considering single photon interaction. In other words, photons leaving the membrane and reflected by the surface of the heater will be directed to the environment, which results in resistance $R_{\infty 2}$ in Fig. C.1. This assumption is based on the fact that the surface of the heater is highly diffusive, and the surface area of the membrane is substantially smaller than the area of the heater. Hence, photons emitted by the membrane and then hit the surface of the heater have minimal chance of being reflected back to the membrane. $R_{\infty b}$ (back side) and $R_{\infty 1}$ (front side) are the radiative thermal resistances between the membrane and the vacuum environment. R_{cond} is the conductive thermal resistance between the membrane and its substrate.

By rearranging the thermal circuit schematic in Fig. C.1(a), we reach the simplified thermal circuit shown in Fig. C.1(b) for which the resistances are expressed as:

$$R_h = \frac{1}{\theta_{rad}\epsilon_m\epsilon_h F}, \tag{C.1}$$

$$R_{\infty,b} = \frac{1}{\theta_{rad}\epsilon_m}, \tag{C.2}$$

$$R_{\infty,1} = \frac{1}{\theta_{rad}\epsilon_m(1-F)}, \tag{C.3}$$

$$R_{\infty,2} = \frac{1}{\theta_{rad}\epsilon_m F(1-\epsilon_h)}, \tag{C.4}$$

$$\theta_{rad} = \frac{4\sigma A_m T_\infty^3}{x_{rad}}. \tag{C.5}$$

where ϵ_m is the total hemispherical emissivity of the SiN membrane, ϵ_h is the total hemispherical emissivity of the ceramic heater, F is the view factor from the membrane to the heater and A_m is surface area of the SiN membrane. We can then combine $R_{\infty b}$, $R_{\infty 1}$, $R_{\infty 2}$ and R_{cond} to be $R_{eq\infty}$ which simplifies to:

$$\frac{1}{R_{eq\infty}} = \theta_{rad}\epsilon_m(2 - F\epsilon_h) + \frac{1}{R_{cond}} \tag{C.6}$$

Then treat the thermal resistors as temperature divider in the thermal circuit:

$$T_m - T_\infty = (T_h - T_\infty) \cdot \frac{G_h}{G_{eq\infty} + G_h}, \tag{C.7}$$

where,

$$G = \frac{1}{R} \tag{C.8}$$

We can further expand Eq. (C.7) to:

$$T_m - T_\infty = (T_h - T_\infty) \cdot \frac{\epsilon_h F}{2 + \frac{1}{R_{cond}\theta_{rad}\epsilon_m}} \tag{C.9}$$

Note that we can express $\frac{1}{R_{cond}\theta_{rad}\epsilon_m}$ as a function of x_{rad} according to:

$$x_{rad} = \frac{G_{rad}}{G_{rad} + G_{cond}} = \frac{2\theta_{rad}\epsilon_m}{2\theta_{rad}\epsilon_m + \frac{1}{R_{cond}}}, \tag{C.10}$$

such that:

$$\frac{1}{R_{cond}\theta_{rad}\epsilon_m} = \frac{2}{x_{rad}} - 2. \tag{C.11}$$

By substituting Eq. (C.11) back to Eq. (C.9), we obtain Eq. (4.32) in the main text.

References

[1] A. Rogalski, "Infrared detectors: Status and trends," *Progress in Quantum Electronics*, vol. 27, no. 2-3, pp. 59–210, 2003.

[2] K. Charles, *Introduction To Solid State Physics, 8th Edition*. Wiley, 2003.

[3] Antoni Rogalski, *Infrared Detectors, 2nd Edition*. CRC Press, 2010.

[4] X. C. Zhang, E. B. Myers, J. E. Sader, and M. L. Roukes, "Nanomechanical torsional resonators for frequency-shift infrared thermal sensing," *Nano Letters*, vol. 13, no. 4, pp. 1528–1534, 2013.

[5] Y. Zhang, Y. Watanabe, S. Hosono, N. Nagai, and K. Hirakawa, "Room temperature, very sensitive thermometer using a doubly clamped microelectromechanical beam resonator for bolometer applications," *Applied Physics Letters*, vol. 108, no. 16, p. 163503, 2016.

[6] A. Blaikie, D. Miller, and B. J. Alemán, "A fast and sensitive room-temperature graphene nanomechanical bolometer," *Nature communications*, vol. 10, no. 1, pp. 1–8, 2019.

[7] M. R. Watts, M. J. Shaw, and G. N. Nielson, "Microphotonic thermal imaging," *Nature Photonics*, vol. 1, no. 11, pp. 632–634, 2007.

[8] B. M. Zwickl, W. E. Shanks, A. M. Jayich, C. Yang, A. C. Jayich, J. D. Thompson, and J. G. Harris, "High quality mechanical and optical properties of commercial silicon nitride membranes," *Applied Physics Letters*, vol. 92, no. 10, pp. 2006–2009, 2008.

[9] P. L. Yu, T. P. Purdy, and C. A. Regal, "Control of material damping in High-Q membrane microresonators," *Physical Review Letters*, vol. 108, no. 8, pp. 1–5, 2012.

[10] S. Chakram, Y. S. Patil, L. Chang, and M. Vengalattore, "Dissipation in ultrahigh quality factor SiN membrane resonators," *Physical Review Letters*, vol. 112, no. 12, pp. 1–5, 2013.

[11] C. Zhang, M. Giroux, T. A. Nour, and R. St-Gelais, "Radiative heat transfer in freestanding silicon nitride membranes," *Physical Review Applied*, vol. 14, p. 024072, Aug 2020.

[12] M. S. Hanay, S. Kelber, A. K. Naik, D. Chi, S. Hentz, E. C. Bullard, E. Colinet, L. Duraffourg, and M. L. Roukes, "Single-protein nanomechanical mass spectrometry in real time," *Nature Nanotechnology*, vol. 7, no. 9, pp. 602–608, 2012.

[13] T. Larsen, S. Schmid, L. G. Villanueva, and A. Boisen, "Photothermal analysis of individual nanoparticulate samples using micromechanical resonators," *ACS Nano*, vol. 7, no. 7, pp. 6188–6193, 2013.

[14] G. Brucoli, P. Bouchon, R. Haïdar, M. Besbes, H. Benisty, and J.-J. Greffet, "High efficiency quasi-monochromatic infrared emitter," *Applied Physics Letters*, vol. 104, no. 8, p. 081101, 2014.

[15] M. Piller, N. Luhmann, M.-H. Chien, and S. Schmid, "Nanoelectromechanical infrared detector," in *Optical Sensing, Imaging, and Photon Counting: From X-Rays to THz 2019*, vol. 11088, p. 1108802, International Society for Optics and Photonics, 2019.

[16] B. M. Zwickl, W. E. Shanks, A. M. Jayich, C. Yang, A. C. Jayich, J. D. Thompson, and J. G. Harris, "High quality mechanical and optical properties of commercial silicon nitride membranes," *Applied Physics Letters*, vol. 92, no. 10, pp. 2006–2009, 2008.

[17] R. St-Gelais, S. Bernard, C. Reinhardt, and J. C. Sankey, "Swept-frequency drumhead optomechanical resonators," *ACS Photonics*, vol. 6, no. 2, pp. 525–530, 2019.

[18] A. Van Herwaarden, D. Van Duyn, B. Van Oudheusden, and P. Sarro, "Integrated thermopile sensors," *Sensors and Actuators A: Physical*, vol. 22, no. 1-3, pp. 621–630, 1990.

[19] A. Van Herwaarden and P. Sarro, "Thermal sensors based on the seebeck effect," *Sensors and Actuators*, vol. 10, no. 3-4, pp. 321–346, 1986.

[20] F. Völklein, "Review of the thermoelectric efficiency of bulk and thin-film materials," *Sensors and Materials*, vol. 8, no. 6, pp. 389–408, 1996.

[21] K. Liddiard, "Thin-film resistance bolometer ir detectors," *Infrared Physics*, vol. 24, no. 1, pp. 57–64, 1984.

[22] A. Tanaka, S. Matsumoto, N. Tsukamoto, S. Itoh, K. Chiba, T. Endoh, A. Nakazato, K. Okuyama, Y. Kumazawa, M. Hijikawa, *et al.*, "Infrared focal plane array incorporating silicon ic process compatible bolometer," *IEEE transactions on Electron Devices*, vol. 43, no. 11, pp. 1844–1850, 1996.

[23] K. Liddiard, "Thin-film resistance bolometer ir detectors—ii," *Infrared physics*, vol. 26, no. 1, pp. 43–49, 1986.

[24] "Saes Group," 2020.

[25] D. R. Lide, *CRC handbook of chemistry and physics*, vol. 85. CRC press, 2004.

[26] M. H. Unewisse, S. J. Passmore, K. C. Liddiard, and R. J. Watson, "Performance of uncooled semiconductor film bolometer infrared detectors," in *Infrared technology XX*, vol. 2269, pp. 43–52, International Society for Optics and Photonics, 1994.

[27] L. Duraffourg, L. Laurent, J.-S. Moulet, J. Arcamone, and J.-J. Yon, "Array of resonant electromechanical nanosystems: a technological breakthrough for uncooled infrared imaging," *Micromachines*, vol. 9, no. 8, p. 401, 2018.

[28] X. C. Zhang, E. B. Myers, J. E. Sader, and M. L. Roukes, "Nanomechanical torsional resonators for frequency-shift infrared thermal sensing," *Nano Letters*, vol. 13, no. 4, pp. 1528–1534, 2013.

[29] G. D. Skidmore, C. Han, and C. Li, "Uncooled microbolometers at drs and elsewhere through 2013," in *Image Sensing Technologies: Materials, Devices, Systems, and Applications*, vol. 9100, p. 910003, International Society for Optics and Photonics, 2014.

[30] V. J. Gokhale and M. Rais-Zadeh, "Uncooled infrared detectors using gallium nitride on silicon micromechanical resonators," *Journal of Microelectromechanical Systems*, vol. 23, no. 4, pp. 803–810, 2013.

[31] T. Yamazaki, S. Ogawa, S. Kumagai, and M. Sasaki, "A novel infrared detector using highly nonlinear twisting vibration," *Sensors and Actuators A: Physical*, vol. 212, pp. 165–172, 2014.

[32] Y. Hui and M. Rinaldi, "High performance nems resonant infrared detector based on an aluminum nitride nano-plate resonator," in *2013 Transducers & Eurosensors XXVII: The 17th International Conference on Solid-State Sensors, Actuators and Microsystems (TRANSDUCERS & EUROSENSORS XXVII)*, pp. 968–971, IEEE, 2013.

[33] W. C. Ang, P. Kropelnicki, H. Campanella, Y. Zhu, A. B. Randles, H. Cai, Y. A. Gu, K. C. Leong, and C. S. Tan, "ALN-based piezoelectric resonator for infrared sensing application," in *Proceedings of the IEEE International Conference on Micro Electro Mechanical Systems (MEMS)*, 2014.

[34] D. Rugar, H. Mamin, and P. Guethner, "Improved fiber-optic interferometer for atomic force microscopy," *Applied Physics Letters*, vol. 55, no. 25, pp. 2588–2590, 1989.

[35] K. J. Lesker, "Kurt J. Lesker Company," 2020.

[36] T. A. Nour, "Custom Vacuum Chamber for Characterization of High Q-factor Silicon Nitride Membrane Resonators," Tech. Rep. April, University of Ottawa, 2019.

[37] Giangrandi.org, "Measuring the Q-factor of a resonator with the ring-down method," 2014.

[38] Digilent, "Analog Discovery 2: 100MS/s USB Oscilloscope, Logic Analyzer and Variable Power Supply," 2020.

[39] T. L. Bergman, F. P. Incropera, D. P. DeWitt, and A. S. Lavine, *Fundamentals of heat and mass transfer*. John Wiley & Sons, 2011.

[40] M. Giroux, "Characterization of a Metal Ceramic Heater Used in a Near-Field Thermophotovoltaic System," Tech. Rep. 8276019, 2019.

[41] C. Zhang, M. Giroux, T. A. Nour, and R. St-Gelais, "Radiative heat transfer in free-standing silicon nitride membranes," *arXiv preprint arXiv:2002.09017*, 2020.

[42] A. Sikora, H. Ftouni, J. Richard, C. Hébert, D. Eon, F. Omnes, and O. Bourgeois, "Highly sensitive thermal conductivity measurements of suspended membranes (sin and diamond) using a 3ω-völklein method," *Review of Scientific Instruments*, vol. 83, no. 5, p. 054902, 2012.

[43] X. Zhang and C. P. Grigoropoulos, "Thermal conductivity and diffusivity of free-standing silicon nitride thin films," *Review of Scientific Instruments*, vol. 66, no. 2, pp. 1115–1120, 1995.

[44] S. G. Volz and G. Chen, "Molecular dynamics simulation of thermal conductivity of silicon nanowires," *Applied Physics Letters*, vol. 75, no. 14, pp. 2056–2058, 1999.

[45] D. J. Wilson, C. A. Regal, S. B. Papp, and H. J. Kimble, "Cavity optomechanics with stoichiometric sin films," *Phys. Rev. Lett.*, vol. 103, p. 207204, Nov 2009.

[46] C. A. Regal and K. W. Lehnert, "From cavity electromechanics to cavity optomechanics," in *Journal of Physics: Conference Series*, 2011.

[47] G. Brucoli, P. Bouchon, R. Haïdar, M. Besbes, H. Benisty, and J.-J. Greffet, "High efficiency quasi-monochromatic infrared emitter," *Applied Physics Letters*, vol. 104, no. 8, p. 081101, 2014.

[48] C. Zhang, M. Giroux, T. A. Nour, and R. St-Gelais, "Thermal radiation sensing using high mechanical Q-factor silicon nitride membranes," in *2019 IEEE SENSORS*, pp. 1–4, oct 2019.

[49] S. E. Zhu, M. Krishna Ghatkesar, C. Zhang, and G. C. Janssen, "Graphene based piezoresistive pressure sensor," *Applied Physics Letters*, vol. 102, no. 16, pp. 2011–2014, 2013.

[50] M. Sansa, E. Sage, E. C. Bullard, M. Gély, T. Alava, E. Colinet, A. K. Naik, L. G. Villanueva, L. Duraffourg, M. L. Roukes, *et al.*, "Frequency fluctuations in silicon nanoresonators," *Nature nanotechnology*, vol. 11, no. 6, p. 552, 2016.

[51] K. Y. Fong, W. H. P. Pernice, and H. X. Tang, "Frequency and phase noise of ultra-high q silicon nitride nanomechanical resonators," *Phys. Rev. B*, vol. 85, p. 161410, Apr 2012.

[52] A. Cleland and M. Roukes, "Noise processes in nanomechanical resonators," *Journal of applied physics*, vol. 92, no. 5, pp. 2758–2769, 2002.

[53] C.-L. Tien and T.-W. Lin, "Thermal expansion coefficient and thermomechanical properties of sin x thin films prepared by plasma-enhanced chemical vapor deposition," *Applied optics*, vol. 51, no. 30, pp. 7229–7235, 2012.

[54] P. Van Zwol, D. Vles, W. Voorthuijzen, M. Péter, H. Vermeulen, W. Van Der Zande, J. M. Sturm, R. W. E. van de Kruijs, and F. Bijkerk, "Emissivity of freestanding membranes with thin metal coatings," *Journal of applied physics*, vol. 118, no. 21, p. 213107, 2015.

[55] B. Revaz, B. Zink, D. O'Neil, L. Hull, and F. Hellman, "Numerical simulation of the heat transfer in amorphous silicon nitride membrane-based microcalorimeters," *Review of scientific instruments*, vol. 74, no. 10, pp. 4389–4403, 2003.

[56] S. Edalatpour and M. Francoeur, "Size effect on the emissivity of thin films," *Journal of Quantitative Spectroscopy and Radiative Transfer*, vol. 118, pp. 75,85, 2013-03.

[57] G. Cataldo, J. A. Beall, H.-M. Cho, B. McAndrew, M. D. Niemack, and E. J. Wollack, "Infrared dielectric properties of low-stress silicon nitride," *Optics letters*, vol. 37, no. 20, pp. 4200–4202, 2012.

[58] H. A. Macleod, *Thin-film optical filters*. CRC press, 2017.

[59] M. H. Sadd, *Elasticity: theory, applications, and numerics*. Academic Press, 2009.

[60] Y. Toivola, J. Thurn, R. F. Cook, G. Cibuzar, and K. Roberts, "Influence of deposition conditions on mechanical properties of low-pressure chemical vapor deposited low-stress silicon nitride films," *Journal of applied physics*, vol. 94, no. 10, pp. 6915–6922, 2003.